Rosenau, M., Lohrmann, J., Oncken, O. (2009): Shocks in a box: An analog model of subduction earthquake cycles with application to seismotectonic forearc evolution. - Journal of Geophysical Research, 114, B01409

DOI: 10.1029/2008JB005665.

Shocks in a box: An analog model of subduction earthquake cycles with application to seismotectonic forearc evolution

Matthias Rosenau[1], Jo Lohrmann[1] and Onno Oncken[1]

We introduce and test an experimental approach to simulate elastoplastic megathrust earthquake cycles using an analog model and apply it to study the seismotectonic evolution of subduction zones. The quasi-two-dimensional analog model features rate- and state-dependent elastic-frictional plastic and viscoelastic material properties and is scaled for gravity, inertia, elasticity, friction and viscosity. The experiments are monitored with a high-resolution strain analysis tool based on digital image correlation (particle imaging velocimetry, PIV) providing deformation time-series comparable to seismologic, geodetic and geologic observations. In order to separate elastic and non-elastic effects inherent the experimental deformation patterns, we integrate elastic dislocation modeling (EDM) into a hybrid approach: We use the analog earthquake slip and interseismic locking distribution as EDM dislocation input and forward model the co- and interseismic elastic response. The residual, which remains when the EDM prediction is subtracted from the experimental deformation pattern, highlights the accumulation of permanent deformation in the model. The setup generates analog earthquake sequences with realistic source mechanisms, elastic forearc response and recurrence patterns and reproduces principal earthquake scaling relations. By applying the model to an accretionary type plate margin we demonstrate how strain localization at the rupture peripheries may lead to a seismotectonically segmented forearc including a tectonically stable shelf and coastal high (< 20 % of plate convergence accommodated by internal shortening) overlying the area of large megathrust earthquake slip. 50

[1] GeoForschungszentrum Potsdam (GFZ), Telegrafenberg, D-14473 Potsdam (Germany)

– 75 % of plate convergence is accommodated by internal shortening in the slope region where earthquake slip tapers out towards the trench. The inner forearc region remains undeformed and represents a basin.

Index terms: 3060 (Subduction zone processes), 8011 (Kinematics of crustal and mantle deformation), 8020 (Mechanics, theory, and modeling), 8104 (Continental margins: convergent), 8123 (Dynamics: Seismotectonics)

1. Introduction

Deformation at active plate margins has two principal components: Elastic deformation testified by megathrust earthquakes and plastic (or permanent) deformation reflected in the tectonic record. Generally, elastic and plastic strains show opposing gradients across subduction zone forearcs [*Byrne et al.,* 1988; *Kelsey et al.*, 1994; *Ruff and Tichelaar*, 1996; *Von Huene and Klaeschen;* 1999; *Song and Simons*, 2003; *Wells et al.*, 2003; *Wang and Hu*, 2006] highlighted by a tectonically rather stable shelf and coastal area overlying the loci of great earthquake slip within the seismogenic zone (Figure 1). Tectonic deformation is accommodated generally outside the areas of great earthquake slip. Where present, an accretionary prism overlying the largely aseismic, shallowest part of the subduction megathrust accommodates the highest fraction of plate convergence-induced shortening in the overriding plate. The temporal evolution of this first-order seismotectonic segmentation of subduction zone forearcs remains, however, enigmatic. Moreover, short-term ($< 10^2$ years time-scale) geodetic and long-term ($> 10^5$ years time-scale) geologic deformation signals rarely resemble each other [e.g. *Khazaradze and Klotz*, 2003] because of the transient (non-linear) nature of seismotectonic deformation patterns generally attributed to elastoplastic [*Wang and Hu*, 2006] and viscoelastic [Wang, 2007] processes (Figure 1). Our understanding of transient seismotectonic forearc evolution substantially benefits from

paleogeodetic techniques [e.g. *Natawidjaja et al.,* 2004] which help closing the gap between short- and long-term observations. However, no model exists so far, that relates tectonic evolution to earthquake cycles and that provides physically self-consistent time-series of deformation comparable to both geodetic and geologic observations [Wang, 2007]. Bridging this gap between short- and long-term is the key to understanding transient deformation signals and the underlying seismotectonic processes.

In the present work we introduce and test an experimental approach to simulate elastoplastic megathrust earthquake cycles using an analog model. We use the model to generate time-series of deformation directly comparable to seismologic, geodetic and geologic observations. We start with the description of the approach including model similarity, material properties, experimental monitoring and deformation analysis. We report first-order experimental observations with respect to analog earthquake source parameters, rupture dynamics, coseismic forearc response and earthquake recurrence and compare the model behavior with nature in order to demonstrate that it generates realistic sequences of analog megathrust earthquakes useful for seismotectonic applications. We finally apply the model to study the link between seismogenic and morphotectonic processes in an accretionary type subduction setting.

2 Experimental Approach

Current models of lithosphere deformation fall into two groups: (1) short-term, elastic and viscoelastic models focusing on seismic cycles, e.g. analog (foam rubber) models [e.g., *Brune*, 1996], analytical [e.g., *Lin and Stein*, 2004] and finite element models [e.g., *Zheng et al*., 1996; *Wang*, 2007], and (2) long-term, plastic models studying tectonic evolution, including sandbox models [e.g., *Lohrmann et al.,* 2003], discrete [e.g., *Vietor and Oncken*, 2005] and finite element models [e.g., *Fuller et al.*, 2006]. Some short-term models consider tectonic deformation as linear

accumulation of permanent deformation superimposed on the elastic or viscoelastic seismic cycles but do not investigate how the tectonic processes involved affect seismic cycles [*Savage*, 1983; *Zheng et al.*, 1996; *Wang*, 2007]. On the other hand, long-term tectonic models do not consider the effects of cyclic stress changes related to earthquakes. Bridging these short- and long-term approaches requires the development of a physically valid seismotectonic model, which should ideally honor earthquake mechanics, elastoplastic and viscoelastic rheologies as well as tectonic driving forces. In practice, designing such a dynamic seismotectonic model is challenging because of the highly non-linear nature of the associated processes: strain- and time-dependency is inherent in the stress loading and relaxation processes [*Wang*, 2007], friction [e.g., *Scholz*, 1998], as well as localization and accumulation of plastic deformation [e.g., *Adam et al.*, 2005]. Moreover, strong variations in the scale of displacement (millimeters to kilometers), time (seconds to millions of years), and deformation rates (km/s to mm/a) requires a model, which is large-scale and of high resolution both in time and space.

Modern analog models featuring realistic rheology and monitored with state-of-the-art analysis tools are capable of generating time-series of deformation at various time scales. Similar to natural observations, the experimental deformation pattern is a superposition of elastic and non-elastic signals (e.g. plastic deformation, inertial effects, etc.). To separate these signals we join analog modeling and elastic dislocation modeling (EDM) into a hybrid approach (Figure 2): By subtracting the EDM-predicted elastic signal from the experimentally observed deformation pattern we derive a residual signal highlighting the non-elastic effects. The present study focuses on phenomena related to elastoplastic deformation processes. Phenomena related to viscoelastic mantle relaxation [*Wang*, 2007, and references therein] are minimized in the presented setup with the aim to reduce complexity of the laboratory observations. We provide a brief discussion of the effects of the interaction of elastoplastic and viscoelastic processes at the end of this paper.

2.1 Model Scaling and Similarity

A scale model of the earth should be geometrically, kinematically and dynamically similar to its natural prototype [*Hubbert*, 1937]. Geometric and kinematic similarity is given if the shape of the model and its deformation rates scale down consistently from nature. Dynamic similarity requires that the ratios of forces, which are expressed as dimensionless numbers, are the same in the model as in the natural prototype. We use the following set of dimensionless numbers to ensure dynamic similarity with respect to gravity, inertia, elasticity, friction and viscosity:

1. The ratio τ between gravitation and strength σ (either frictional or viscous) is

$$\tau = \rho \cdot l \cdot g / \sigma \qquad (1)$$

where ρ is the rock density, l is a characteristic length, and g is the gravitational acceleration.

2. The Froude Number relates gravitation and inertia and is

$$Fr = v \cdot (g \cdot l)^{-0.5} \qquad (2)$$

where v is a characteristic velocity.

3. The Cauchy Number relates inertia and elasticity and is

$$Ca = \rho\, v^2 / k \qquad (3)$$

where k is the bulk modulus.

By keeping these dimensionless numbers the same in an experiment executed in the earth's gravity field as in nature, the following scaling relationships are derived from equations (1) to (3):

$$\tau^* = \tau \;\rightarrow\; (\sigma^*/\sigma) = (\rho^*/\rho) \cdot (l^*/l) \qquad (4)$$

$$Fr^* = Fr \;\rightarrow\; (t^*/t) = (l^*/l)^{0.5} \qquad (5)$$

$$Ca^* = Ca \;\rightarrow\; (k^*/k) = (\rho^*/\rho) \cdot (l^*/l)^2 \cdot (t/t^*)^2 \qquad (6)$$

where * marks the model numbers and values. The dimensionless ratios between model and natural prototype quantities are known as the scaling factors.

Granular materials used here are three times less dense than their natural counterparts (i.e. $(\rho^*/\rho) = 0.33$) and models are designed at a length scale $(l^*/l) = 3.3 \cdot 10^{-6}$ such that 1 cm in the model corresponds to 3 km in nature. From equation (4) it follows that the models have to be weaker by

a factor (σ^*/σ) = $1.1 \cdot 10^{-6}$. The properties controlling the brittle strength are cohesion C and the friction coefficient μ. Cohesion has the same dimension like strength (unit Pa) and thus scales down with the same factor (C^*/C) = $1.1 \cdot 10^{-6}$. The friction coefficient is dimensionless and thus scales with a factor (μ^*/μ) = 1. The properties controlling viscous strength are strain rate (unit s^{-1}) and viscosity η (unit Pas). Scaling of viscosity thus depends on the time scale. Keeping the Froude number constant (equation (5)) requires that for a length scale (l^*/l) = $3.3 \cdot 10^{-6}$ the temporal scaling factor has to be (t^*/t) = $1.8 \cdot 10^{-3}$ (i.e. 0.1 second in the lab corresponds to about 50 seconds in nature). Since it is unsuitable for simulating long-term processes, we use this scale only for modeling the earthquake process itself (coseismic time scale) where inertial forces may be important. Under the assumption that inertial forces may not play an important role during slow, tectonic deformation we scale the interseismic time separately with a factor of $1.3 \cdot 10^{-10}$ (i.e. 1 second in the lab is about 250 years in nature) more suitable for laboratory realization. Having set this interseismic time scale, the viscosity scale follows as the product of interseismic time and stress scale: (η^*/η) = $1.4 \cdot 10^{-16}$. Note that in the experiments viscosity is consequently not properly scaled at the coseismic time scale. We justify this by the assumption that the earth's mantle is viscoelastic, i.e. responds mainly elastic during an earthquake and viscously during slower deformation [*Wang*, 2007]. Finally, from equation (6) and using the scaling factors for density, length and coseismic time scales as defined above, the scaling factor for the bulk modulus follows (k^*/k) = $1.1 \cdot 10^{-6}$. The presented model does not include the effects of erosion, sedimentation and isostatic compensation of topography.

2.2 Material Properties

Our analog subduction zone models (e.g. that in Figure 3 and described in detail below) include an elastic-frictional plastic (elastoplastic) continental lithosphere made of granular material

composed of mixtures of rice, sugar, rubber pellets and a viscoelastic continental asthenosphere made of silicone oil. Frictional properties of granular experimental materials (cohesion *C*, internal friction coefficient μ, friction rate parameter *a*-*b*) have been measured using a Schulze ring shear tester RST-01.pc [*Schulze*, 1994]. We performed dynamic friction tests at variable normal load and variable shear rate (velocity stepping tests). Elasticity of experimental materials has been measured using a uni-axial compression tester. We performed loading-unloading cycles and derived the bulk modulus *k* during loading after initial compaction. The rheology of liquid material has been characterized using a cone-plate rheometer (Rheotec RC20.1-CPS-P1 with C25-2 measurement system) equipped with a Peltier element to control temperature during analysis. We measured the viscosity with controlled shear rates and studied the viscoelastic behavior in creep and relaxation tests. All material tests as well as the analog experiments have been performed at constant temperature (23°C) and dry room climate (30-40 % humidity) controlled by an air conditioning system.

2.2.1 Frictional Properties

Unstable (seismic) stick-slip and stable (aseismic) slip behavior are generally described in terms of a rate and state friction law [e.g., *Scholz*, 1998, and references therein]. This constitutive law includes a friction rate parameter "*a*-*b*" which describes the velocity dependence of friction (the rate effect): for $a-b < 0$, the frictional strength decreases with increasing slip velocity (velocity weakening behavior) resulting in a slip instability associated with a stress drop. Earthquakes are slip instabilities and seismogenic zones are described as velocity weakening regimes. For $a-b > 0$, the frictional strength increases with increasing slip rate (velocity strengthening behavior) such that earthquake nucleation is inhibited. Aseismic zones of the subduction interface are described as velocity strengthening regimes. The state effect of the rate and state friction law describes the

dependency of frictional strength on the age of the fault interface: the longer the fault interface is held in contact, the larger its strength.

Slip surfaces developed in rice show unstable slip under experimental conditions and has been used to mimic megathrust earthquakes within the seismogenic zone of the subduction plate interface. The main "coseismic" deformation mechanism is particle boundary sliding. The frictional interfaces of rice undulate at wavelengths of meters to hundreds of meters and amplitudes of decimeters to meters if scaled to nature, which we consider similar to natural fault roughness [*Rosenau et al*., 2008].

Slip surfaces developed in rice show a remarkably regular stick-slip pattern resulting in a saw-tooth-like time-stress curve with stress drops occurring periodically every 2 – 3 seconds under experimental conditions (Figure 4a). Stress drops are followed by elastic and inelastic stress build-up. Pre-failure stress build-up is controlled by accelerating slip and weakening resulting in "blunting" of the saw-tooth pattern. Increasing the normal load results in longer recurrence intervals as well as larger absolute and fractional stress drops (Figure 4b). Increasing the shear rate has opposite effects.

We have been able to reproduce both the rate and state effect of friction using rice (Figure 4c and d). Accordingly, the stick-slip behavior of rice reflects intrinsic velocity weakening. The slope of the negative correlation of friction coefficient with shear rate is consistent with a friction rate parameter a-b of about -0.015 similar to the values of rocks [e.g., *Scholz*, 1998, and references therein]. However, the logarithmic trend of fractional stress drop with normal load (Figure 4b) indicates that a-b may actually be normal load-dependent. The trend suggests that a-b increases by at least an order-of-magnitude from "seismogenic depth" to the surface. This is consistent with results from laboratory friction experiments using clay material under conditions representative

for the shallowest part of subduction megathrusts [*Saffer et al.,* 2001*; Saffer and Marone*, 2003]. A positive correlation between recurrence intervals and stress drops of stick-slip events (Figure 4d) mimics the aging of natural faults, i.e. the state effect of friction.

Slip surfaces developed in refined sugar shows stable slip under experimental conditions and has been used to simulate aseismic slip. The results of velocity stepping tests demonstrate the velocity strengthening frictional behavior of sugar (Figure 4c). The kinked slope of the positive correlation between shear rate and friction coefficient is consistent with a friction rate parameter *a*-*b* of about +0.02 at low velocities (< 0.01 mm/s) and +0.01 at higher velocities. Accordingly, sugar is very similar to serpentinite [*Reinen et al.,* 1994], which is thought to control the mechanical behavior of the subduction megathrust where it is in contact with the hydrated lithospheric mantle wedge of the continental plate [*Oleskevich et al.,* 1999]. Cohesion of all granular materials used here are in the order of 10 Pa scaling up to about 9 MPa in nature.

2.2.2 Elastic Properties

The granular materials have been mixed with rubber pellets (Melos® EPDM-Granules 0.5 – 1.5 mm diameter) to yield desired and properly scaled elastic effects. For low strains, rubber pellets are linearly elastic with a bulk modulus of 0.1 MPa (Figure 5a). Elasticity of composite granular materials (e.g. rice-rubber-mix, sugar-rubber-mix) is dominated by the elasticity of rubber for mixtures containing more than 50 vol.-% rubber pellets (Figure 5b). A bulk modulus of about 0.1 MPa for the model lithosphere scale up to about 90 GPa in nature. Densities of composite granular materials are 900 kg/m³, which correspond to 2800 kg/m³ in nature.

2.2.3 Viscoelastic Properties

Silicone oil (MOMENTIVE PERFORMANCE MATERIALS Baysilone® SE30) is a modified Maxwell material with a power law viscous rheology at experimental conditions. We have used it to simulate the ductile flow of the asthenospheric mantle wedge at the base of the continental plate. In this study, which focuses on the near-field deformation of the forearc lithosphere, we have chosen a viscoelastic material with rather weak non-linearity and short relaxation time in order to minimize the effect of viscoelastic relaxation of the model asthenosphere. At experimental temperatures (23°C) and strain rates (0.1 - 1 s^{-1}), the effective viscosity of silicone oil used is about 10^4 Pas (scaling up to $7 \cdot 10^{19}$ Pas in nature) and weakly stress-dependent (power law stress exponent n = 1.3, Figure 6a). Figure 6b shows its viscoelastic relaxation behavior during a creep test mimicking loading during an analog earthquake: The almost straight trend of the creep curve after instantaneous ("coseismic") elastic deformation is consistent with a Maxwell rheology including a minor non-linear component and a short Maxwell relaxation time (scaling up to about a month in nature). Density of silicone oil is 1000 kg/m³ corresponding to about 3100 kg/m³ in nature.

2.3 Experimental Setup and Conditions

The experimental setup used in this study is a modification of conventional quasi-two-dimensional sandbox setups [e.g., *Lohrmann et al.*, 2003] monitored from one side with an industrial strain analysis system (particle imaging velocimetry, PIV). The experiment consists of a glass-sided box (100 cm long, 50 cm high and 10 cm wide) in which the analog model is set up (Figures 2 and A1). A basal conveyer plate is connected to a constantly motor-driven piston via a spring loaded thrust pad (i.e. a power-joint originally used to connect a sailing rig with a windsurf board). Thus the conveyer plate is allowed to store elastic energy while being pulled. We consider this loading procedure reasonable in mimicking the plate tectonic driving forces active at the

spatial scale of our interest. The velocity of the conveyer plate is monitored by a high-resolution electronic odometer at micrometer precision (frequency = 1 kHz).

The generalized subduction zone model presented here is reminiscent of a 300-km-long section of forearc lithosphere between the trench and backarc (Figure 3). We simplified the subduction geometry by considering a 15° dipping megathrust between a ~ 60-km-thick, initially flat topped elastoplastic forearc lithosphere and an elastic oceanic plate including a 100-km-wide seismogenic zone (Figure 3). We consider a seismogenic zone characterized by velocity weakening behavior with a downdip decreasing friction rate parameter. It is limited downdip by the transition to velocity strengthening behavior similar to subduction zones like Chile and Alaska [*Oleskevich et al.,* 1999]. The downdip limit is defined by the material transition from rice (velocity weakening) to sugar (velocity strengthening) along the base of the model.

The model forearc wedge is "plate tectonically" loaded by pulling the conveyer plate via the power-joint at a constant rate of about 0.07 mm/s equivalent to about 77 mm/a in nature. Analog earthquakes nucleate spontaneously within the seismogenic zone during loading and release (part of) the elastic strain energy stored in the system. Rather fast "coseismic" slip rates cause a strength drop within the velocity weakening seismogenic zone whereas the strength of the plate interface downdip of the seismogenic zone increases due to its velocity strengthening behavior (Figure 3). The relative strength drop within the seismogenic zone decreases also in the updip direction. This results in a strength minimum at a "seismogenic depth" and an updip strength gradient similar to the shallow coseismic strengthening proposed for natural subduction zones [*Wang and Hu*, 2006; *Wang and He*, 2008]. During the "interseismic" period, at low slip rates, the strength of the model seismogenic zone recovers and is relatively larger than the strength of

the downdip part of the plate interface. Thus we have realized analog model strength profiles which are transient at seismic cycle scales.

2.4 Experimental Monitoring and Deformation Analysis

2.4.1 Particle Imaging Velocimetry (PIV)

Detection of analog earthquakes and cross-sectional strain analysis of the model during experimental runs is performed by using an optical deformation monitoring system (particle imaging velocimetry, PIV Strainmaster by LaVision, Germany; see *Adam et al.* [2005] for a comprehensive description of this application in analog geodynamic modeling). LaVision's PIV Strainmaster is an industrial tool which allows high-resolution strain field measurements of solid, granular and fluid flows employing digital imaging techniques in combination with texture correlation analysis (Figure A1). During a model run, the locations of particles are recorded by sequential digital images of a 12-bit monochrome charged-coupled device camera acquired at a frequency of 10 Hz. The particle motions between successive images are then determined by cross-correlation of textural differences (i.e. gray values) formed by groups of particles within interrogation windows using a Fast Fourier Transform algorithm. Based on the resultant displacement vector field, local derivative calculations finally provide the cross-sectional components of the strain tensor.

2.4.2 Monitoring Resolution and Precision

PIV precision is a function of the image resolution (i.e. pixel size), texture quality (e.g. contrast) and cross-correlation parameters (interrogation window size, shape and overlap). Under favorable conditions PIV is able to detect displacements at micrometer precision. Using 64 x 64 pixel-sized interrogation windows, we track the particle displacements during experiments with a precision

of about 5 μm (scaling up to 1.5 meters in nature). A window overlap of 87 % results in a spatial resolution of 4 x 4 mm (scaling up to 1200 x 1200 m). The accuracy of the derived strain field is generally better than 0.01 %.

2.4.3 Derivation of Analog Earthquake Source Parameters and Deformation Time-Series

From the detected cross-sectional deformation field of sequential images, time-series of the incremental deformation are derived. During visual inspection of the deformation time-series, we identify analog earthquakes as recurrent events with deformation rates orders-of-magnitude faster than the "interseismic" signal. The image acquisition rate is sufficiently high (10 Hz) to catch single events as they rupture along the plate interface providing two successive images of the associated deformation field (we call such events "split-events" because they are cut into two increments, see Figure A1). From the "coseismic" increments, we derive the two-dimensional source parameters of analog earthquakes by means of basal shear (slip) and rupture length as well as the coseismic wedge response by means of particle motions and surface deformation. From cross-correlation of the first and the last image of the "interseismic" period, we derive the interseismic deformation field by means of basal shear (or locking) and associated wedge deformation. To analyze transient deformation signals, we use incremental deformation time-series with a temporal resolution large enough to detect deformation and small enough to subdivide the seismic cycle into several increments (generally, one-second-increments result in a tenfold subdivision of an analog seismic cycle). The finite deformation field is derived by cross-correlating images which span time intervals of tens of seismic cycles (generally > 100 seconds). By this, we assure that the observed deformation likely do not include elastic effects and reflect solely permanent deformation.

2.4.4 Elastic Dislocation Modeling (EDM)

We have incorporated an elastic dislocation modeling approach in order to separate elastic and non-elastic signals of the laboratory observed deformation pattern (Figure 2). In particular, we use the experimentally generated and PIV-derived slip distributions as dislocation input into an elastic dislocation model (EDM) and calculate the ideal elastic response of the model lithosphere to the imposed slip. Coseismic megathrust slip is put into the EDM as forward slip. Interseismic megathrust slip constrains the EDM according to the backslip concept [*Savage*, 1983]: Backslip would be the amount of plate convergence during the interseismic interval for a kinematically locked megathrust (i.e. no interseismic slip) and zero for a megathrust slipping at plate convergence rate. The residual which remains when the calculated elastic response is subtracted from the observed elastoplastic deformation field highlights the non-elastic effects.

For elastic dislocation modeling, we used Coulomb 3.1 [*Toda and Stein,* 2002*; Lin and Stein*, 2004]. Coulomb calculates deformation in an elastic halfspace with uniform and isotropic elastic properties following *Okada* [1992]. To allow direct comparison between analog and elastic dislocation models used here, the elastic properties and geometries of the EDMs (Poisson´s ratio = 0.3, Young's modulus = 110 GPa) are similar to the analog model if scaled to nature. We use a planar megathrust with 3-km-wide dislocations. To ease comparison of the models and nature, we display the experimentally observed and EDM-predicted surface deformation patterns at the natural scale.

3 Model Performance

Here we describe the analog model behavior and compare our observations to nature in order to provide a test for model predictions and assess its applicability for further applications. In total, we performed more than 30 experiments systematically varying experimental conditions and model parameters to study and improve the performance of the setup.

During a 15-minute experimental run the models compact and evolve from those dominated by plastic deformation to those dominated by elastic deformation. Whereas the earliest stages of dominantly plastic wedge evolution (< 5 minutes) may have no natural prototype, the middle stages of evolution may be comparable to the behavior of accretionary margins where a still significant amount of plate convergence has been accommodated by shortening of the overriding plate (e.g. Southern Chile, Alaska, Sumatra). The late stages may represent the mainly elastic behavior of non-accretionary and erosive margins (e.g. Northern Chile, Japan). Although only a limited number of the world's subduction zones are accretive today, we want to focus on this type of margin in the present study because they may play a key role in seismotectonic evolution. To show a representative behavior, the following analysis focuses on 51 analog earthquakes which occurred successively during the mid-part of the experimental run no. 29 (Figure 7). We refer to this five-minute long sequence as "sequence 29". Experimental parameters will be scaled to nature where useful for comparison with natural observations. Most analog earthquakes of sequence 29 each occurred within the 0.1 second time window of sequential PIV monitoring providing insights into the static coseismic source parameters and forearc deformation. Six analog earthquakes of sequence 29 have been split into two parts by the sequential PIV ("split-events") providing additional insights into rupture dynamics. These "quasi-dynamic" observations are accompanied by high resolution "source-time functions" detected by the odometer which monitors the velocity of the conveyer plate.

3.1 Earthquake Source Parameters

The analog megathrust earthquakes are characterized by asymmetric shear motion and a slightly skewed, bell-shaped slip distribution (Figure 8) consistent with natural and numerically simulated subduction earthquakes [e.g., *Wang and He*, 2008]. Average "coseismic" slips of sequence 29

range from 7 to 62 μm with a mean of 27 ± 16 μm (1σ standard deviation), or about 8 ± 5 meters in nature. Maximum slip is up to 90 μm. Rupture widths of sequence 29 analog earthquakes varies from 30 to 350 mm. A positive correlation between analog earthquake shear and rupture width (Figure 9a) is consistent with the slip-length scaling behavior of earthquakes [e.g., *Scholz*, 2002, chapter 4]. Most events overlap in their rupture area with prior and following events but isolated events occur as well (e.g. event no. 18). Sub-sequences with systematic gap filling events occur (e.g. events no. 1-3, 10-13 and 43-45 of sequence 29). Generally, such subsequences of events initiate at the lower part of the seismogenic zone and migrate upwards.

3.2 Magnitude Scaling

In order to compare experimental observations with natural earthquakes by means of stress drop and magnitude scaling relations, we scaled the analog two-dimensional source parameters to three-dimensional source parameters with the following procedure: From data for subduction earthquakes compiled by *Cloos* [1992] an empirical scaling law of the form

$$rupture\ length = 6.5 \cdot slip^{1.2} / rupture\ width \qquad (7)$$

has been derived. We used this empirical power law to estimate a theoretical rupture length from the observed slip and rupture width assuming uniform slip along strike. As this scaling law yields unrealistically high rupture lengths (> 3000 km) and therefore magnitudes (> M10) for earthquakes with average slips exceeding about 10 meters (the data compiled by *Cloos* [1992] are for earthquake slips < 8 m), we additionally applied a saturation condition: Scaled rupture lengths

are limited to 1300 km which corresponds to a mean maximum length of possible earthquakes in subduction zones of the earth [*McCaffrey*, 2008]. Under this condition, scaled moment magnitudes of sequence 29 events range from M8.3 to M9.5. Noticeably, the slopes of the correlations between the scaled seismic moment with rupture width and coseismic slip (Figure 9b) are very similar to large earthquakes in nature [e.g., *Lay and Wallace*, 1995, chapter 9]. Applying a circular crack model [*Lay and Wallace*, 1995, chapter 9], the coseismic stress drop can be calculated from the static two-dimensional source parameters. Accordingly, stress drops during analog megathrust earthquakes of sequence 29 range from 1 to about 40 Pa. These would scale up to stress drops of 1-50 MPa in nature, which is consistent with typical stress drops during subduction earthquakes [*Wang and Hu*, 2006; and references therein].

3.3 Rupture Kinematics and Mechanisms

From events saturating the 35 cm wide seismogenic zone of the model within the 0.1 s time window of sequential PIV monitoring, a minimum rupture velocity of 3.5 m/s can be derived. Accompanying experiments with variable width of the seismogenic zone suggest that rupture velocities in the model are typically about 5 m/s corresponding to 3 km/s in nature. This is similar to rupture velocities during earthquakes [e.g., *Scholz*, 2002, chapter 4].

Events which have been cut into two increments (split-events) shed light on the rupture modes. Generally, such split-events show overlapping rupture areas with the second increment being wider than the first consistent with an expanding crack-like rupture mode (Figure 7). Most ruptures nucleate near the base of the seismogenic zone and propagate updip guided by the "lithostatic" pressure gradient [*Das and Scholz*, 1983]. Some events, however, also propagate downdip to a limited distance into the velocity strengthening zone. Split event no. 7 of sequence 29 is an example of a crack-like rupture propagating up- and downdip. Except for this crack-like

event, split-events of sequence 29 show migrating incremental slip maxima. These incremental slip maxima propagate closely behind the rupture front indicating a pulse-like rupture mode overprinted onto the general crack-like rupture mode (such split-events are marked as mixed mode in Figure 7). Split event no. 45 is the one closest to a pure pulse-like rupture as indicated by a propagating asperity and minimal overlapping incremental rupture areas.

The dominance of ruptures with a pulse character in the split event catalog of sequence 29 (5 of 6) may not necessarily mean that analog earthquakes propagate dominantly as pulses. Actually the opposite may be true since slip pulses are believed to propagate slower than cracks [*Lykotrafitis et al.,* 2006] and therefore have a higher probability of being "caught in the act" by sequential PIV monitoring. Cracks may simply be too fast to be observed incrementally. The overall rarity of split-events in the whole catalog (6 of 51 events) thus actually suggests a dominance of crack-like rupture mechanisms. Although, natural observations with respect to subduction earthquake dynamics are limited, the experimental behavior seems to be consistent with the few recent observations of natural megathrust earthquakes [e.g., *Krüger and Ohrnberger*, 2005, *Robinson et al.,* 2006] in that they spread updip and to a limited degree downdip as cracks from the deep end of the seismogenic zone.

3.4 Source Time Functions

The source time functions of analog earthquakes have been approximated by the coseismic motion of the conveyer plate monitored by the odometer (Figure 10). Accordingly, static offsets of the conveyer plate are in the order of ten micrometers consistent with near-fault particle motions in the downgoing plate inferred from PIV analysis (Figure 8a). The critical slip distance, which is the offset that occurs until the highest ("seismic") slip rates are reached, is a few micrometers which is in the scale of surface irregularities of the granular material (i.e. rice) used

(Figure 4b). The rise time, which we define as the time of analog earthquake slip acceleration, is about one third of the total (two-dimensional) rupture duration. From successive differentiation of the slip-time function, we inferred near fault particle velocities within the slab of about 1 mm/s and accelerations of about 0.3 m/s². Note that near-fault particle velocity and acceleration in the overriding plate have to be much higher because larger displacements occur in the hanging wall during the same time interval. The experimentally observed critical slip distances and rise times scale up to natural values in the order of decimeters to meters and a few seconds, respectively, which reasonably fit earthquake observations [e.g., *Hirose and Shimamoto*, 2005].

3.5 Coseismic Forearc Response

The static coseismic forearc deformation pattern of the analog model is characterized by "seaward" motion above the rupture area (Figure 8). Horizontal velocities at the surface are in the order of decimeters per second if scaled to nature similar to ground motions during great earthquakes like the 2004 Sumatra-Andaman earthquake [*Subarya et al.,* 2006]. Slip along the megathrust causes extension and compression at the downdip and updip limit of the rupture, respectively. The surface response to this volumetric strain is subsidence and uplift, respectively. Comparison with the surface deformation pattern predicted by an EDM, where the experimentally observed slip distribution is used as dislocation input, shows a first-order similarity. From this similarity we infer that the upper-plate response to analog earthquake slip is mainly elastic. Second-order differences are evident such as more localized uplift and a shift of the inflection point separating uplift from subsidence. To date we cannot decide whether these are artifacts of one of the models (e.g. due to the elastic halfspace approximation of the EDM calculation) or geological meaningful observations (e.g. localized uplift due to faulting in the upper plate). However, the surface deformation pattern is largely consistent with the differential uplift and

subsidence of subduction zone forearcs observed for historical megathrust earthquakes [*Plafker*, 1972; *Meltzner et al*., 2006].

3.6 Earthquake Recurrence

Sequence 29 includes 51 detected analog earthquakes with recurrence intervals ranging from 1.2 to 11.4 seconds (Figure 11a). The scaled natural recurrence times range between 300 – 2850 years. Because of our limited observation span and accuracy in nature, a reliable determination of return times of great earthquakes has not been made [*McCaffrey*, 2008]. The model recurrence intervals match to recurrence times derived from frequency simulations of great earthquake in subduction zones [*McCaffrey*, 2008]. The mean analog earthquake recurrence interval is well defined (5.9 ± 2.1 seconds, 1σ standard deviation). The recurrence frequency, however, does not fit a normal distribution (Figure 11b). Instead, a bimodal distribution appears with a group of less frequent great events ($M > 9$ if scaled to nature) and a group of more frequent $M < 9$ events.

To further characterize the experimental recurrence behavior, we may analyze inherent strain-dependencies. In this context, we only consider the elastic strain controlled by the rate of tectonic loading and release during earthquakes. The simplest model of strain-dependent earthquake recurrence is the perfectly elastic seismic cycle [*Reid*, 1910]. In this model "characteristic" earthquakes of constant size occur periodically at constant time intervals (i.e. a normalized recurrence close to one in Figure 11b) and the fault cycles between an upper and lower strain level [*Ellsworth*, 1995]. This model applies very well to analog earthquakes generated during ring shear testing where a regular stick-slip behavior is observed (Figure 4a). This periodic or characteristic behavior is likely due to the perfectly elastic setup in combination with fixed loading and release conditions during ring shear testing: A constant shear velocity and normal load assures constant loading and a prescribed rupture area assures a constant release rate. In the

subduction zone model setup, neither perfectly elastic behavior nor fixed loading and release conditions do exist. Instead plastic wedge deformation may modify the loading conditions and the rupture area is not prescribed resulting in a more complex, non-characteristic recurrence behavior.

For non-characteristic behavior, Reid´s model has been modified into time- and slip-predictable models [*Shimazaki and Nakata*, 1980]. A time-predictable model has an upper strain threshold, so the time to the next earthquake is determined by the size of the last earthquake, or in other words, the more strain released in an earthquake, the longer it will take to build up the required strain for the next. Slip-predictable models have a lower threshold, so the time elapsed since the past earthquake determines the size of the next event: the longer the interseismic period continues, the larger the next earthquake will be. To justify a slip- or time-predictable model, earthquake size should correlate positively with the length of the preceding or subsequent interseismic interval, respectively. For sequence 29 events, we found no correlation of analog earthquake size with preceding interseismic time. A weak correlation of analogue earthquake size with subsequent interseismic time (Figure 11c) may justify a time-predictable model. Closer inspection of the strain energy curve (Figure 11a) reveals that sub-sequences of sequence 29 events may well follow a slip- or time-predictable or even a characteristic model for a limited number of seismic cycles (try to fit incremental linear upper and lower bounds to the curve). This transient strain-dependent behavior can also be inferred from a local densification of the lines connecting successive events in a plot like Figure 11c.

A rather well-defined mean earthquake recurrence time observed experimentally is consistent with paleoseismological records of Sumatra [*Natawidjaja et al.,* 2004], Chile [*Bookhagen et al.,* 2006], Japan [*Shimazaki and Nakata*, 1980], Alaska and New Zealand [*Lajoie, 1986*, and

references therein]. Paleoseismological records from Japan additionally justify, at least for the time-scale of observation (a few seismic cycles), a time-predictable recurrence model [*Shimazaki and Nakata*, 1980]. The model observation suggests, however, that even in a rather simple setting (i.e. one single large fault) we might not expect a long-term stable recurrence pattern defined by more than a few successive events.

4 Model Application to Seismotectonic Forearc Evolution

Much effort has recently put on the correlation of forearc anatomy (i.e. structure and morphology) and slip during great subduction earthquakes to provide a tool relevant to seismic hazard mapping based on long-term geological and geophysical observations [*Byrne et al.*, 1988; *Kelsey et al.*, 1994; *Ruff and Tichelaar*, 1996; *Von Huene and Klaeschen,* 1999; *Song and Simons*, 2003; *Wells et al.*, 2003; *Fuller et al*., 2006; *Wang and Hu*, 2006]. Regarding the first-order anatomy of subduction forearcs and its relation to megathrust earthquakes, the dynamic Coulomb wedge theory [*Wang and Hu,* 2006] provides the fundamental framework of seismotectonic evolution. The theory states that coseismic stress buildup at the tip of megathrust earthquake ruptures is the principal driving force of deformation within the outermost part of the forearc wedge often associated with an accretionary prism. To test this prediction and to get first-order insights into the genetic link between seismogenic and morphotectonic processes in megathrust settings, we apply our model to accretionary subduction zones. We expect the tectonic signal of earthquake cycles to be greatest in these settings where a relatively large fraction of plate convergence is taken up by shortening within the overriding plate: Offshore Alaska about 70 % of plate convergence has been accommodated within the accretionary prism [*Von Huene and Klaeschen*, 1999] whereas the shelf area behaves dominantly elastic. In Southern Chile the Pliocene to recent inversion of shelf basins and rapid uplift of the coastal area evidence that

significant shortening of the shelf and coastal area may occur at least transiently in such settings [*Bookhagen et al*., 2008; *Melnick and Echtler*, 2006; *Melnick et al.*, 2006]. Cross-forearc shortening associated with rapid surface uplift is also evident in the geologic record of the northern Sumatra-Andaman margin [*Fisher et al.,* 2007; *Rajendran et al.,* 2008].

4.1 Coupling

Forearc deformation is driven by plate convergence and cyclic stress fluctuation associated with megathrust earthquakes [*Wang and Hu*, 2006]. To explore the interaction between these driving forces we first have to investigate their relative proportions in a more kinematic sense using the concept of "coupling" [*Wang and Dixon*, 2004]. Accordingly, plate convergence may be partitioned into three components:

$$\textit{plate convergence} = \textit{seismic slip} + \textit{aseismic slip} + \textit{tectonic shortening}. \quad (8)$$

4.1.1 Seismic Coupling

The fraction of plate convergence taken up by seismic slip is the "seismic coupling coefficient":

$$\chi = \textit{seismic slip} / \textit{plate convergence.} \quad (9)$$

χ may vary from 0 (aseismic subduction) to 1 (pure stick-slip). Apart from the physical properties of the subduction megathrust, derivation of χ from observations depends on the size of the smallest earthquakes included in its calculation. Generally the smallest earthquakes included correspond to the magnitude of completeness of a specific seismic record. Based on a magnitude of completeness of M5.5, *Frohlich and Wetzel* [2007] suggested that in subduction zones in average about one-third of plate convergence is released seismically. In our simulations including earthquakes larger than M8.5 if scaled to nature, only about one-tenth of convergence is released "seismically". Using the Gutenberg-Richtenberg frequency-size relationship of earthquakes [e.g. *Lay and Wallace*, 1995, chapter 9] we can scale the experimentally derived χ to the conditions of the analysis of *Frohlich and Wetzel* [2007]: Assuming a b-value (the slope in the Gutenberg-Richter distribution) of 0.65 to 1 and a three order-of-magnitude difference in completeness, the experimentally detected seismic coupling coefficient ($\chi = 0.1$) may then correspond to $\chi = 0.3$-0.4 consistent with the analysis of *Frohlich and Wetzel* [2007].

4.1.2 Locking (Geodetic Coupling)

Interseismically, kinematic coupling between the plates is described by the "geodetic coupling" or "locking coefficient" λ, which is the fraction of plate convergence accumulating as elastic and plastic strain in the overriding plate, or in other words, the fraction of plate convergence not accommodated by aseismic slip between great earthquakes:

$$\lambda = 1 - \textit{aseismic slip} / \textit{convergence.} \qquad (10)$$

Although little is known about the state of interseismic locking and megathrust slip in nature, it may be reasonable to assume that a significant amount of plate convergence is taken up by interseismic slip in the seismogenic zone: A growing body of evidence from geodetic and seismological studies [*Arnadottir et al*., 1999; *Freymueller et al.,* 2000; *Bilek and Lay*, 2002; *Ozawa et al*., 2002; *Haberland et al*., 2006; *Hsu et al*., 2006; *Lange et al.,* 2007; *McCaffrey et al.*, 2008, *Tréhu et al*., 2008] indicate that shallow (less than about 30 km deep) interseismic megathrust slip may occur at least locally and transiently. Moreover, exhumed accretionary mélanges along ancient subduction channels show clear evidence for significant ductile (and presumably aseismic) deformation down to seismogenic depth [e.g., *Shreve and Cloos*, 1988; *Remitti* et al., 2007; *Vanucchi et al*., 2008].

In our experiments, interseismic slip varies systematically both in space and time: Mean interseismic slip increases downdip from less than half of the convergence rate in the "seismogenic zone" ($\lambda > 0.5$) to plate convergence rate ($\lambda = 0$) at greater depth (Figure 13). Within the "seismogenic zone" interseismic slip accelerates steadily from close-to-zero directly after an analog earthquake ($\lambda > 0.9$) to about two third of the convergence rate ($\lambda = 0.33$, Figure 12a). Note that in the experiment we cannot distinguish between "aseismic" slip and slip corresponding to analog earthquakes below our detection limit (about M8.5 if scaled to nature)

4.2 Accumulation of Permanent Deformation Throughout Seismic Cycles

4.2.1 Interseismic Forearc Deformation

The interseismic model forearc deformation pattern is characterized by "landward" motions above the seismogenic zone (Figure 13) roughly inverse to the coseismic deformation field (Figure 8). Particle velocities at the surface are about one third of the plate convergence rate

similar to what is observed along the coast of Southern Chile [*Khazaradze and Klotz*, 2003; *Wang et al.*, 2007] and Sumatra [*Chlieh et al.*, 2008]. Spatially heterogeneous locking at depth cause localized compression and uplift of the model outer forearc. Comparison with an EDM suggests that a major portion of the experimental deformation is plastic (Figure 13). A bimodal surface uplift pattern and the particle motions suggest that plastic strain is accommodated along "seaward" and "landward" vergent shear zones, which we interpret as proto-thrusts. The subsidence seen in the model inner forearc may be related to elastic loading by and underthrusting beneath the outer forearc. Note that interseismic subsidence compensates coseismic uplift of the inner forearc seen in the experiment. Mean interseismic uplift rates are in the order of millimeters per year if scaled to nature similar to interseismic coastal uplift rates in Southern Chile [*Khazaradze and Klotz*, 2003; *Wang et al.*, 2007] and Sumatra [*Chlieh et al.*, 2008].

4.2.2 Transient Deformation Patterns

To interpret the deformation patterns by means of driving forces, we investigate transient signals of interseismic deformation in the experiments using incremental (1 second) time-series of horizontal shortening. Figure 14 shows these time-series at positions equivalent to the slope-to-shelf transition and the coastal area in nature. Accordingly, the near-trench shortening rate is close to zero (within limits of PIV detection) during most of the experimental interseismic period (Figure 14a). We therefore conclude that the plastic shortening at this position seen in the cumulative deformation pattern of Figure 13 accumulates within the one-second-increment of the foregoing analog earthquake. Likely this "postseismic" deformation is driven by coseismic compression at the rupture tip. Near-trench shortening may therefore be viewed as a postseismic relaxation mechanism consistent with the dynamic Coulomb wedge theory. The model coastal

shortening rate is low throughout the interseismic interval (about 0.4 microstrain per year if scaled to nature, Figure 14b). A more precise time-series (0.1 s increments) of coastal uplift in Figure 12b indicates that experimental interseismic uplift accelerates. Assuming that shortening rate remains constant, accelerating uplift may reflect strain localization along with the transition from distributed elastic loading early in the interseismic period to accumulation of plastic strain along the proto-backthrust late in the interseismic period.

4.2.3 Finite Deformation Pattern

Figure 15 is a synoptic view of the model forearc anatomy and its relation to cumulative megathrust earthquake slip as it evolved over the 50 simulated seismic cycles of sequence 29. The finite deformation pattern is characterized by localized wedge shortening at the updip and downdip limits of cumulative analog earthquake slip at its base. Finite strain in the model upper crust peaks close to the trench where shortening is accommodated presumably by a proto-thrust zone. Here about 50 - 75 % of plate convergence is accommodated similar to what is proposed for Alaska [*Von Huene and Klaeschen*, 1999]. Permanent shortening of the upper crust decreases significantly landward to less than 20 % of plate convergence. It shows a subordinate peak in the modal coastal area reflecting strain localization along the proto-backthrust which marks the downdip limit of the “seismogenic zone”. The distribution of shortening causes uplift of the area overlying the areas of cumulative slip during analog megathrust earthquakes and morphological segmentation of the model outer forearc into a flat “shelf” and dipping “slope”. The model inner forearc is a largely undeformed, topographic low separated from the outer forearc by a “coastal high”. Surface uplift rates are in the order of millimeters per year if scaled to nature and correspond to long-term uplift rates along the most rapidly rising coasts of the world, e.g. that of Southern Chile and the Nicobar-Andaman Islands north of Sumatra [*Lajoje*, 1986; *Bookhagen et*

al., 2006; *Melnick et al.*, 2006; *Rajendran et al*., 2008]. Note that the surface uplift rates as well as the finite morphology of the analog model may differ from natural examples because important processes controlling topographic evolution in nature (erosion, sedimentation, isostacy) are not included in our simulation.

5 Discussion, Implications and Conclusions

5.1 Interaction of Elastoplastic and Viscoelastic Deformation

The elastoplastic deformation transients observed experimentally may occur in nature along with viscoelastic mantle relaxation. Interaction may result in more complex deformation patterns and different deformation rates than those simulated here on all time-scales. Viscoelastic mantle relaxation is a large-scale postseismic process which relieves coseismic stresses imposed on the oceanic and continental asthenosphere [*Wang*, 2007]. The most prominent viscoelastic signal can be expected during the decades following an earthquake and encompasses the entire forearc, arc and backarc region. High postseismic coastal uplift rates as well as trenchward motion of the backarc region are observable signals in nature [e.g., *Khazaradze and Klotz*, 2003; *Wang*, 2007, and references therein] generally attributed to this process. How does elastoplastic deformation modify this pattern? Our experimental observations suggest that the postseismic coastal uplift signal related to elastoplastic reloading is close to zero (Figure 12b). High postseismic coastal uplift rates observed in nature may therefore be exclusively related to viscoelastic mantle relaxation and only weakly "contaminated" by an elastoplastic effect (Figure 16). Later during the seismic cycle, however, the signal of the viscoelastic relaxation effect diminishes (Figure 1) whereas the elastoplastic loading signal accelerates (Figure 12b). Therefore late interseismic coastal uplift rates are likely controlled by the process of elastoplastic reloading. The interaction of viscoelastic relaxation and elastoplastic reloading may thus result in a decelerating-

accelerating interseismic uplift signal in coastal areas similar to that shown schematically in Figure 16. On the long time-scale, however, we do not expect a significant contribution of viscoelastic effects to tectonic evolution.

5.2 Relationship Between Megathrust Earthquakes and Forearc Anatomy

Our simulation demonstrates consistent with the dynamic Coulomb wedge concept that stress changes associated with megathrust seismic cycles can have first-order control on the anatomy of a subduction zone. Importantly, forearc structure and morphology may therefore be used to constrain the rupture area of great megathrust earthquakes. It is suggested that the slope-to-shelf transition marks the updip limit of the megathrust slip during great earthquakes. Uplift here may occur due to shortening accommodated by accretionary wedge thrusts or out-of-sequence, splay faults [*Park et al*., 2002; *Henstock et al*., 2006]. Whatever the thrusting mechanism, our model, in accord with the dynamic Coulomb wedge theory, suggests that reactivation of such faults is a relaxation mechanism driven by coseismic compression and causes a symptomatic postseismic uplift transient (Figure 16). Transient interseismic thrusting events within the accretionary wedge have been detected recently in Japan [*Davis et al.*, 2006; *Ito and Obara*, 2006]. Complementary to postseismic uplift at the slope-to-shelf transition late interseismic plastic shortening at the downdip limit of the seismogenic zone may lead to uplift of a coastal high with respect to the inner forearc basin (Figure 15). Because great earthquakes mainly nucleate deep within the seismogenic zone [*Das and Scholz*, 1983], this may explain why subduction earthquake hypocenters generally line-up along the coast [*Ruff and Tichelaar*, 1996]. Summarizing the above inferences, the slope-to-shelf transition and the transition from the coastal high to the inner forearc basin may be used as a first-order, cross-sectional proxy for a long-term "characteristic" earthquake size in a specific setting useful for seismic hazard assessment.

Based on the seismotectonic segmentation we observed experimentally, we speculate that strain localization at the rupture periphery may also apply in three dimensions: Depending on the rupture mechanisms of lateral propagating earthquake ruptures and their relation to the plate motion vector, a long-term control of the seismogenic process on morphotectonic evolution similar to what we observed experimentally in cross-section may result in along-trench seismotectonic segmentation. The coincidence of peninsulas with segment boundaries (e.g. the Arauco and Mejillones peninsulas in Chile) may be controlled by such a process.

At a smaller scale than the first-order segmentation given by the seismogenic zone limits and segment boundaries, heterogeneous coseismic slip may be capable of localizing strain around single asperities. In settings where asperities are persistent features, this may lead to a seismotectonic sub-segmentation of the margin over multiple seismic cycles. Such a seismotectonic sub-segmentation is suggested by the global correlation between forearc basins and asperities as inferred from gravity anomalies reported by *Song and Simons* [2003] and *Wells et al.* [2003].

To conclude, the dynamic Coulomb wedge concept and the study presented here provide a physically plausible explanation of how seismogenic processes can control the morphotectonic evolution of subduction forearcs. This complements the idea of forearc structure controlling seismogenesis [e.g., *Fuller et al*., 2006]. A discussion of possible feedback loops is clearly beyond the scope of the present paper but by merging the existing ideas, coupling of morphotectonic and seismogenic processes appears as a viable, self-sustaining mechanism resulting in a long-term correlation between forearc anatomy and coseismic megathrust slip.

Appendix:

Figure A1.

Notation

a'	coseismic slip acceleration, m/s².
a-b	friction rate parameter.
A	source area, m².
C	cohesion, Pa.
Ca	Cauchy Number.
d	shear zone thickness, m.
D	coseismic slip, m.
Fr	Froude Number.
g	gravitational acceleration, m/s².
G	gravitation, N.
η	viscosity, Pas.
h	depth, m.
I	inertia, N.
λ	locking coefficient.
l	characteristic length, m.
L	dimension of length.
k	bulk modulus, Pa.
M	moment magnitude.
M_0	seismic moment, Nm.
M	dimension of mass.
n	power law stress exponent.
r	source radius, m.
S	scaling factor.
ρ	density, kg/m³.
t	characteristic time, s.
$\Delta\tau$	stress drop, Pa.
τ_f	frictional shear strength, Pa.
τ_v	viscous shear strength, Pa.
T	dimension of time.
T_{rel}	Maxwell relaxation time, s.
μ	friction coefficient.
v	characteristic velocity, m/s.
V	rock volume, m³.
χ	seismic coupling coefficient.

Acknowledgements

We thank Guenther Tauscher, Frank Neumann, and Thomas Ziegenhagen for engineering and technical assistance, Rainer Nerlich, Henrich Zierbes, Martin Stange, and Lisa Pech for material testing. Thanks to Jürgen Adam, Georg Dresen, Silvan Hoth, Nina Kukowski, Kerstin Schemmann and Bernd Schurr for stimulating discussions. We are grateful to Kelin Wang, an anonymous reviewer, Jeffrey J. McGuire, and Patrick Taylor for constructive reviews of the manuscript and helpful comments. Research has been funded by the German Ministry of Education and Research (BMBF) and the German Research Foundation (DFG), grant 03G0594 (to M.R.) and GFZ Potsdam. This is publication no. GEOTECH-319 of the R&D-Program GEOTECHNOLOGIEN.

References

Adam, J., et al. (2005), Shear localisation and strain distribution during tectonic faulting - New insights from granular-flow experiments and high-resolution optical image correlation techniques, *Journal of Structural Geology*, *27*, 183-301, doi:10.1016/j.jsg.2004.08.008.

Arnadottir, T., Thornley, S., Pollitz, F. F., and D. J. Darby (1999), Spatial and temporal strain rate variations at the northern Hikurangi margin, New Zealand, *Journal of Geophysical Research, 104*, 4931-4944, paper number: 1998JB900109.

Bilek, S. L., and T. Lay (2002), Tsunami earthquakes possibly widespread manifestations of frictional conditional stability, *Geophysical Research Letters*, *29*, doi: 10.1029/2002GL015215.

Bookhagen, B., Echtler, H. P., Melnick, D., Strecker, M. R., and J. Q. G. Spencer (2006), Using uplifted Holocene beach berms for paleoseismic analysis on the Santa Maria Island, south-central Chile, *Geophysical Research Letters, 33*, doi:10.1029/2006GL026734.

Brune, J. N. (1996), Particle motion in a physical model of shallow angle thrust faulting, *Proceedings of the Indian Academy of Science (Earth and Planetary Sciences), 105*(2), 197-206.

Byrne, D. E., Davis, D. M., and L. R. Sykes (1988), Loci and maximum size of thrust earthquakes and the mechanics of the shallow region of subduction zones, *Tectonics, 7,* 833-857.

Chlieh, M., Avouac, J. P., K. Sieh, K., Natawidjaja, D. H., and J. Galetzka (2008), Heterogeneous coupling of the Sumatran megathrust constrained by geodetic and paleogeodetic measurements*, Journal of Geophysical Research, 113*, doi:10.1029/2007JB004981.

Cloos, M. (1992), Thrust-type subduction-zone earthquakes and seamount asperities: a physical model for seismic rupture, *Geology*, *20*, 601-604.

Davis, E. E., et al. (2006), A discrete episode of seismic and aseismic deformation of the Nankai trough subduction zone accretionary prism and incoming Philippine Sea plate, *Earth and Planetary Science Letters, 242*, 73-84, doi: 10.1016/j.epsl.2005.11.054

Das, S., and C. H. Scholz (1983), Why large earthquakes do not nucleate at shallow depths, *Nature*, *305*, 621-623.

Ellsworth, W. L. (1995), Characteristic earthquakes and long-term earthquake forecasts: implications of central California seismicity, in *Urban Disaster Mitigation: The role of Science and Technology,* edited by Cheng, F. Y. and M. S. Sheu, Elsevier, Oxford.

Fisher, D., Mosher, D., Austin Jr., J. A., Gulick, S. P. S., Masterlark, T., and K. Moran (2007), Active deformation across the Sumatran forearc over the December 2004 M_w9.2 rupture, *Geology 35*, 99-102, doi: 10.1130/G22993A.1.

Freymueller, J. T., Cohen, S. C., and H. J. Fletcher (2000), Spatial variations in the present-day deformation, Kenai Peninsula, Alaska, and their implications, *Journal of Geophysical Research, 105,* 8079-8101, paper number: 1999JB900388.

Fuller, C. W., et al. (2006), Formation of forearc basins and their influence on subduction zone earthquakes, *Geology*, *34*, 65-68, doi: 10.1130/G21828.1.

Haberland, C., et al. (2006), Interaction between forearc and oceanic plate at the south-central Chilean margin as seen in local seismic data, *Geophysical Research Letters*, *33* (5) doi: 10.1029/2006GL028189.

Henstock, T. J., et al. (2006), Seafloor morphology of the Sumatran subduction zone: Surface rupture during megathrust earthquakes? *Geology*, *34*(6), 485-488, doi: 10.1130/22426.1.

Hirose, T., and T. Shimamoto (2005), Slip-Weakening Distance of Faults during Frictional Melting as Inferred from Experimental and Natural Pseudotachylytes, *Bulletin of the Seismological Society of America, 95*(5)*,* 1666-1673, doi: 10.1785/0120040131.

Hsu, Y. J., et al. (2006), Frictional afterslip following the 2005 Nias-Simeulue earthquake, Sumatra, *Science*, *312*, 1921-1926, doi: 10.1126/science.1126960.

Hubbert, M. K. (1937), Theory of scale models as applied to the study of geological structures, *Geological Society of America Bulletin, 48,* 1459–1520.

Ito, Y., and K. Obara (2006), Dynamic deformation of the accretionary prism excites very lowfrequency earthquakes, *Geophysical Research Letters*, *33*, doi: 10.1029/2005GL025270.

Kelsey, H. M., Engebretson, D. C., Mitchell, C. E., and R. L. Ticknor (1994), Topographic form of the Coast Ranges of the Cascadian Margin in relation to coastal uplift rates and plate subduction, *Journal of Geophysical Research, 99,,* 12245-12255, paper number: 93JB03236.

Khazaradze, G., and J. Klotz (2003), Short- and long-term effects of GPS measured crustal deformation rates along the south central Andes, *Journal of Geophysical Research-Solid Earth*, *108* (B6), doi: 10.1029/2002JB001879.

Krüger, F., and M. Ohrnberger (2005), Tracking the rupture of the Mw = 9.3 Sumatra earthquake over 1,150 km at teleseismic distance, *Nature*, *435*, 937-939, doi:10.1038/nature03696.

Lajoie, K. R. (1986), Coastal Tectonics, in *Active Tectonics, Studies in Geophysics,* pp. 95-124, , National Academic Press, Washington, D. C., USA.

Lange, D., Rietbrock, A., Haberland, C., Bataille, K., Dahm, T., Tilmann, F., and E. R. Flüh (2007), Seismicity and geometry of the south Chilean subduction zone (41.5°S–43.5°S): Implications for controlling parameters, *Geophysical Research Letters, 34*, doi: 10.1029/2006GL029190.

Lay, T. and T. C. Wallace (1995), *Modern Global Seismology*, *International Geophysics Series, 58*, 521 pp., Academic Press Limited, London, UK.

Lin, J., and R.S. Stein (2004), Stress triggering in thrust and subduction earthquakes and stress interaction between the southern San Andreas and nearby thrust and strike-slip faults, *Journal of Geophysical Research 109*, doi: 10.1029/2003JB002607.

Lohrmann, J., et al. (2003), The impact of analogue material properties on the geometry, kinematics, and dynamics of convergent sand wedges, *Journal of Structural Geology*, *25*, 1691-1711.

Lykotrafitis, G., et al. (2006), Self-healing pulse-like shear ruptures in the laboratory, *Science*, *313*, 1765-1768, doi: 10.1126/science.1128359.

McCaffrey, R. (2008), Global frequency of magnitude 9 earthquakes, *Geology, 36,* 263-266, doi: 10.1130/G24402A.1.

McCaffrey, R., Wallace, L. M., and J. Beavan (2008), Slow slip and frictional transition at low temperature at the Hikurangi subduction zone, *Nature Geoscience, 1,* 316-320, doi:10.1038/ngeo178.

Melnick, D., and H. Echtler (2006), Inversion of forarc basins in south-central Chile caused by rapid glacial age trench fill, *Geology, 34*, 709-712, doi: 710.1130/G22440.22441.

Melnick, D., Bookhagen, B., Echtler, H.P., and M. R. Strecker (2006), Coastal deformation and great subduction earthquakes, Isla Santa María, Chile (37°S), *GSA Bulletin, 118*, 1463-1480, doi: 10.1130/B25865.1

Meltzner, A. J., K. Sieh, M. Abrams, D. C. Agnew, K. W. Hudnut, J. Avouac, D. H. Natawidjaja (2006), Uplift and subsidence associated with the great Aceh-Andaman earthquake of 2004, *Journal of Geophysical Research*, *111*, doi: 10.1029/2005JB003891.

Moore, G. F., Bangs, N.L., Taira, A., Kuramoto, S., Pangborn, E., and H.J. Tobin (2007), Three-Dimensional Splay Fault Geometry and Implications for Tsunami Generation, *Science 318*, 1128-1131, doi: 10.1126/science.1147195.

Natawidjaja, D. H., et al. (2004), Paleogeodetic records of seismic and aseismic subduction from central Sumatran microatolls, Indonesia, *Journal of Geophysical Research*, *109*, doi: 10.1029/2003JB002398.

Okada, Y. (1992), Internal deformation due to shear and tensile faults in a halfspace, *Bull. Seismol. Soc. Am., 82,* 1018– 1040.

Oleskevich, D. A., et al. (1999), The updip and downdip limits to great subduction earthquakes: Thermal and structural models of Cascadia, south Alaska, SW Japan, and Chile, *Journal of Geophysical Research*, *104*, 14965-14991, paper number 1999JB900060.

Ozawa, S., et al. (2002), Detection and monitoring of ongoing aseismic slip in the Tokai region, central Japan, *Science, 298*, 1009-1012, doi: 10.1126/science.1076780.

Park, J. O., et al. (2002), Splay fault branching along the Nankai subduction zone, *Science*, *297*, 1157-1160.

Plafker, G., 1972, Alaskan earthquake of 1964 and Chilean earthquake of 1960: Implications for arc tectonics, *Journal of Geophysical Research, 77*, 901-925.

Rajendran, K., et al. (2008), Age estimates of coastal terraces in the Andaman and Nicobar Islands and their tectonic implications, *Tectonophysics, 455*, 53-60, doi:10.1016/j.tecto.2008.05.004

Reid, H.F. (1910), On mass-movements in tectonic earthquakes, in *The California earthquake of April 18, 1906: Report of the state earthquake investigation commission*, Carnegie Institute of Washington, D.C., USA.

Reinen, L. A., et al. (1994), The frictional behavior of lizardite and antigorite serpentinites: experiments, constitutive models, and implications for natural faults, *Pure and Apllied Geophysics*, *143*, 317-358, paper number: 0033-4553/94/030317.

Remitti, F., Bettelli, G., and P. Vannucchi (2007), Internal structure and tectonic evolution of an

underthrust tectonic mélange: the Sestola-Vidiciatico tectonic unit of the Northern Apennines, Italy, *Geodinamica Acta, 20*(1-2), 37-51.

Robinson, D. P., et al. (2006), Earthquake rupture stalled by a subducting fracture zone, *Science*, *312*, 1203-1205, doi: 10.1126/science.1125771.

Rosenau, M., Oppelt, A., Kemnitz, H., and O. Oncken (2008): Analogue earthquakes: Friction experiments with rice and implications for the seismic cycle and earthquake nucleation, *Bolletino di Geofisica 49.*

Ruff, J. R., and B. W. Tichelaar (1996), What controls the seismogenic plate interface in subduction zones? in *Subduction: Top to Bottom, Geophysical Monograph 96,* edited by G. E. Bebout et al., pp. 105-111, *AGU, USA.*

Saffer, D. M., Frye, K. M., Marone, C., and K. Mair (2001), Laboratory results indicating complex and potentially unstable frictional behaviour of smectite clay, *Geophysical Research Letters 28*, 2297-2300,.

Saffer, D. M., and C. Marone (2003), Comparison of smectite- and illite-rich gouge frictional properties: Application to the updip limit of the seismogenic zone along subduction megathrusts, *Earth and Planetary Science Letters 215*, 219-235, doi:10.1016/S0012-821X(03)00424-2

Savage, J. C. (1983), A dislocation model of strain accumulation and release at a subduction zone, *Journal of Geophysical Research, 88*(B6), 4984-4996.

Shreve, R. L., and M. Cloos (1986), Dynamics of sediment subduction, melange formation, and prism accretion, *Journal of Geophysical Research, 91,* 10229–10245.

Schulze, D. (1994), Entwicklung und Anwendung eines neuartigen Ringschergerätes, *Aufbereitungstechnik 35*(10), 524-535.

Scholz, C. H. (1998), Earthquakes and friction laws, *Nature*, *391*, 37-42.

Scholz, C. H. (2002), *The Mechanics of Earthquakes and Faulting*, 2nd ed., 471 pp., Cambridge Univ. Press, Cambridge.

Shimazaki, K., and T. Nakata (1980), Time-predictable recurrence model for large earthquakes, *Geophysical Research Letters*, *7*, 279–282.

Song, T. R. A., and M. Simons (2003), Large trench-parallel gravity variations predict seismogenic behavior in subduction zones, *Science*, *301*, 630-633.

Subarya, C., et al. (2006), Plate-boundary deformation associated with the great Sumatra-Andaman earthquake, *Nature, 440*, 46-51, doi: 10.1038/nature04522.

Toda, S., and R. S. Stein (2002), Response of the San Andreas fault to the 1983 Coalinga-Nuñez Earthquakes: An application of interaction-based probabilities for Parkfield, *Journal of Geophysical Research* , *107,* doi: 10.1029/2001JB000172.

Tréhu, A. M., Braunmiller, J., and J. L. Nabelek (2008), Probable low-angle thrust earthquakes on the Juan de Fuca–North America plate boundary, *Geology 36*(2), 127-130, doi: 10.1130/G24145A.1.

Vannucchi, P., Remitti, F., G. Bettelli (2008), Geological record of fluid flow and seismogenesis along an erosive subducting plate boundary, *Nature 451*(7)*,* 699-703, doi: 10.1038/nature06486.

Vietor, T., and O. Oncken (2005), Controls on the shape and kinematics of the Central Andean plateau flanks: Insights from numerical modelling, *Earth and Planetary Science Letters, 236*, 814-827, doi: 10.1016/j.epsl.2005.06.004.

Von Huene, R., and D. Klaeschen (1999), Opposing gradients of permanent strain in the aseismic zone and elastic strain across the seismogenic zone of the Kodiak shelf and slope, Alaska, *Tectonics*, *18*, 248-262, paper number: 1998TC900022.

Wang, K. (2007), Elastic and viscoelastic models of crustal deformation in subduction earthquake cycles, in *The Seismogenic Zone of Subduction Thrust Faults, MARGINS Theoretical and Experimental Earth Science Series*, edited by T. H. Dixon and J. C. Moore, Columbia Univ. Press, New York, USA.

Wang, K., and T. Dixon (2004), "Coupling" semantics and science in earthquake research, *Eos, 85*, 180-181.

Wang, K., and Y. Hu (2006), Accretionary prisms in subduction earthquake cycles: The theory of dynamic Coulomb wedge, *Journal of Geophysical Research, 111,* doi: 10.1029/2005JB004094.

Wang, K. and J. He (2008), Effects of frictional behaviour and geometry of subduction fault on coseismic seafloor deformation, *Bulletin of the Seismological Society of America 98,* 571-579, doi: 10.1785/0120070097.

Wang, K., Hu, Y., Bevis, M., Kendrick, E., Smalley Jr.,R., Vargas., R.B., Lauría, E. (2007), Crustal motion in the zone of the 1960 Chile earthquake: Detangling earthquake-cycle deformation and forearc-sliver translation, *G3, 8*, doi:10.1029/2007GC001721.

Wells, R. E., et al. (2003), Basin-centered asperities in great subduction zone earthquakes: A link between slip, subsidence, and subduction erosion? *Journal of Geophysical Research, 108*, doi: 10.1029/2002JB002072.

Zheng, G., Dmowska, R., and J.R. Rice (1996), Modeling earthquake cycles in the Shumagin subduction segment, Alaska, with seismic and geodetic constraints, *Journal of Geophysical Research, 101*(B4), 8383-8392, paper number: 95JB03461.

Captions

Figure 1. Spatiotemporal distribution of elastic and plastic deformation observed in subduction zone forearcs. Short-term deformation patterns reflect seismic cycle strain and viscoelastic mantle relaxation. Long-term patterns reflect the effect of plastic strain localization and accumulation. Interaction of elastoplastic and viscoelastic deformation adds complexity to both the short- and long-term signals.

Figure 2. Hybrid analog-elastic dislocation model approach. An analog experiment (terms referring to the natural prototype are italic) is monitored using a strain analysis tool based on cross-correlation of sequential images (particle imaging velocimetry, PIV). PIV-derived analog earthquake slip distribution is used as dislocation input into an elastic dislocation model (EDM). By subtracting the EDM-predicted elastic deformation signal from the PIV-derived signal we obtain a residual signal highlighting the plastic deformation.

Figure 3. Analog subduction zone model. Terms referring to the natural prototype and values scaled to nature are italic. The slip rate and strength profiles along the basal "megathrust" show the cyclic loading conditions and associated strength fluctuations realized during the experiment. See notation in the appendix for abbreviations used.

Figure 4. Rate- and state-dependent frictional properties of analog materials: (a) Typical "blunted saw-tooth" stress-time curve during regular stick-slip of rice at experimental conditions (normal load = 1 kPa, shear rate = 0.08 mm/s). (b) Correlation between fractional stress drop and normal load (error bars indicate variation). (c) Rate effect of friction: Velocity weakening and strengthening behavior of rice and sugar, respectively (a-b derived by linear regression, 1σ-standard deviation indicated by error bars). Friction coefficients have been derived from velocity

stepping tests by linear regression of 10 doublet measurements at 1 – 10 kPa normal load. (d) State effect of friction of rice: Correlation between recurrence time and stress drop of stick-slip events during a velocity stepping test (normal load = 5 kPa).

Figure 5. Elastic properties of analog materials: (a) Axial stress-strain curve during un-axial compression test (overlay of multiple loading cycles following initial compaction) of EPDM pellets indicating a linear elastic behavior. The slope corresponds to a bulk modulus of 0.1 MPa. (b) Bulk modules of composite granular materials (sugar-rubber = black squares, rice-rubber = black squares) as a function of fraction of rubber (error bars are standard deviations from triplet measurements). Note the non-linear mixing trend indicating the dominant influence of rubber on bulk elastic properties.

Figure 6. Rheology of analog material: (a) Viscous yield strength (open triangles) and viscosity (closed squares) of silicone oil as functions of shear rate at room temperature (23°C). (b) Creep test result of silicone oil indicating its Maxwell viscoelastic behavior (imposed shear stress = 1 kPa).

Figure 7. Simplified slip distribution of 51 successive analog earthquakes of sequence 29. Black bars mark the total extent of the rupture area. Stars mark the loci of maximum slip. Split events are bracketed (rupture mode propagation direction indicated by arrow). Numbers refer to events discussed in the text.

Figure 8. Synoptic view of coseismic model forearc deformation (surface uplift and particle velocities; vertical extent of the lines indicate PIV precision) and comparison with the prediction of an elastic dislocation model (EDM) where the basal slip distribution has been used as

dislocation input (error bars indicate PIV precision). Terms referring to the natural prototype and values scaled to nature are italic.

Figure 9. Scaling relations of analog megathrust earthquakes of sequence 29: (a) Average shear vs. rupture width. (b) Scaled slip-moment and rupture width-seismic moment relations. Split events appear as outliers because they are plotted with their incremental slip and rupture area. The vertical and horizontal linear trends for large events in (a) and (b), respectively, are the effect of saturation of the seismogenic zone. Terms referring to the natural prototype and values scaled to nature are italic.

Figure 10. Example of source time function of an analog earthquake as detected by the odometer monitoring the conveyer plate ("slab") motion: (a) displacement versus time, (b) velocity versus time, (c) acceleration versus time.

Figure 11. Recurrence behavior of analog earthquakes in sequence 29: (a) Elastic strain energy release pattern. Vertical drops indicate strain release during analog earthquakes approximated by the slip distance. Sloped portions indicate strain accumulation between earthquakes at a linear accumulation rate equal to the mean release rate of the sequence. (b) Distribution of recurrence intervals normalized by the average recurrence (a perfectly periodic behavior would be indicated by a normalized recurrence of 1). (c) Magnitude vs. recurrence time calculated as the time to the subsequent event (lines connect successive events).

Figure 12. Experimental deformation time-series showing (a) slip rate history of the model megathrust shown as cumulative shear and (b) uplift history of the model coastal area over sequence 29 (time-series integrate 0.1 s time increments; "eq" denotes earthquakes). Visible steps

correspond to very great (scaled M > 9 if scaled to nature) events. Note the transient signals on various time-scales.

Figure 13. Synoptic view of interseismic model forearc deformation (surface uplift and particle velocities; vertical extent of the lines indicate PIV precision) and comparison with the prediction of an elastic dislocation model (EDM) where the basal distribution of locking has been used as dislocation input (backslip; error bars indicate PIV precision). Terms referring to the natural prototype and values scaled to nature are italic.

Figure 14. Incremental time-series of model forearc shortening rates during sequence 29 (one-second-increments; shortening is positive and calculated over 4 mm distances) at the "slope-to-shelf-transition" (a) and in the "coastal area" (b) ("eq" denotes earthquakes).

Figure 15. Synoptic view of the finite forearc anatomy (topography, upper crustal shortening and particle displacement field) after the 50 seismic cycles of sequence 29 and its relation to coseismic megathrust slip. The "slope-to-shelf" transition is located at the position where cumulative coseismic megathrust slip tapers out "trenchward" and where repeated coseismic compression drives postseismic shortening along a proto-thrust. A proto-backthrust related to the downdip limit of the seismogenic zone accumulates late interseismic plastic shortening and cause uplift of a "coastal high". Terms referring to the natural prototype and values scaled to nature are italic.

Figure 16. Hypothetical transient deformation signals resulting from the interaction of elastoplastic loading/relaxation of the lithosphere and viscoelastic mantle relaxation. Transient signals are shown schematically as time-series of uplift at the slope-to-shelf transition and coastal high ("eq" denotes earthquakes).

Figure A1. Workflow of experimental strain analysis using particle imaging velocimetry (PIV): Sequential images of model side views are correlated based on pattern recognition within overlapping interrogation windows using a Fast Fourier Transform algorithm. The result is a particle displacement field at sub-pixel accuracy. Local derivate calculations finally provide the cross-sectional strain tensor. Inset shows how PIV may split earthquakes into two increments ("split events").

Table Caption:

Table 1. Analog model parameters, material properties, experimental conditions, scaling and similarity. See notation in the appendix for abbreviations used.

	Parameters: Quantity	Symbol	Dimension {M,L,T}	Unit	**Similarity:** Quantitiy	Model		Nature		Dimensionless number	Scaling factor	
Model parameters	Length	l	L	[m]	mean coseismic slip critical slip distance	0.027 2	mm µm	8 0.6	m m		$3.3 \cdot 10^{-6}$	Geometric similarity
	Time (interseismic)	t	T	[s]	mean recurrence interval	5.9	s	1475	a		$1.3 \cdot 10^{-10}$	Kinematic similarity
	Time (coseismic)				rupture duration rise time	0.01 0.003	s s	5 2	s s		$1.8 \cdot 10^{-3}$	
	Velocity (interseismic)	v	L/T	[m/s]	plate velocity	0.064	mm/s	77	mm/a		$2.6 \cdot 10^{-4}$	
	Velocity (coseismic)				slip velocity rupture velocity	2 5	mm/s m/s	1 3	m/s km/s		$1.8 \cdot 10^{-3}$	
	Graviational acceleration Coseismic slip acceleration	g a'	L/T^2	[m/s^2]		9.81 0.6	m/s² m/s²	9.81 0.6	m/s² m/s²	g/a'		Dynamic similarity
	Friction coefficient	µ				0.7		0.7		φ	1	
	Friction rate parameter	a-b			velocity weakening velocity strengthening	-0.015 +0.015		-0.015 +0.015		a-b		
	Cohesion	C	M/LT^2	[Pa]		10	Pa	9	MPa		$1.1 \cdot 10^{-6}$	
	Seismic coupling coefficient	χ				0.1		0.1		χ	1	
Material properties	Bulk modulus	k	M/LT^2	[Pa]		0,1	MPa	93	GPa		$1.1 \cdot 10^{-6}$	
	Viscosity	η	M/LT	[Pas]		10^4	Pas	$7 \cdot 10^{19}$	Pas		$1.4 \cdot 10^{-16}$	
	Maxwell relaxation time	T_{rel}	T	[s]		0.5	ms	0.1	a		$1.3 \cdot 10^{-10}$	
	Stress exponent	n				1.3		1.3		n	1	
	Density	ρ	M/L^3	[kg/m^3]	lithosphere asthenosphere	900 1000	kg/m^3 kg/m^3	2800 3111	kg/m^3 kg/m^3		0.33	
Forces	Gravitation Inertia	$G = \Theta Vg$ $I = \Theta Va$	ML/T^2	[N]						$Fr = v[gl]^{-0.5}$ $Ca = \rho v^2/k$	$1.2 \cdot 10^{-17}$	
Energy	Seismic moment	$M_0 = kDA$	ML^2/T^2	[Nm]	mean	10^{-1}	Nm	10^{21}	Nm		$4 \cdot 10^{-23}$	
Stresses	Frictional shear strength	$\tau f = C + \varphi\rho gh$	M/LT^2	[Pa]	maximum	628	Pa	586	MPa	$\tau = \rho hg/C$	$1.1 \cdot 10^{-6}$	
	Viscous shear strength	$\tau v = \eta\, vi/d$				64	Pa	60	MPa			

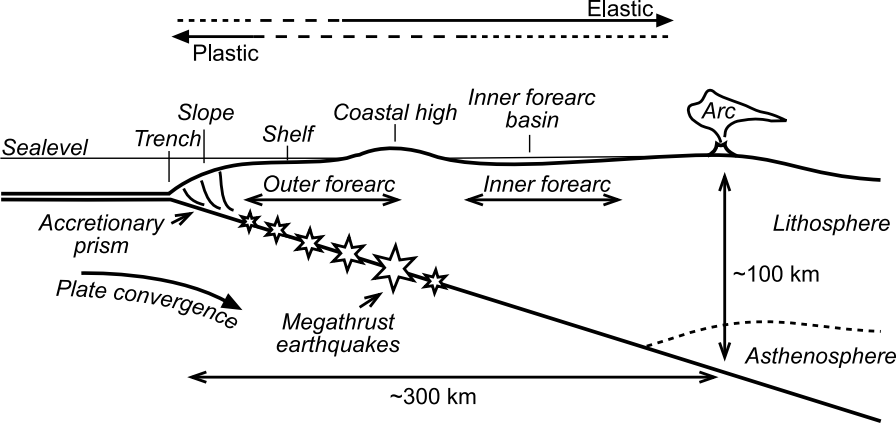

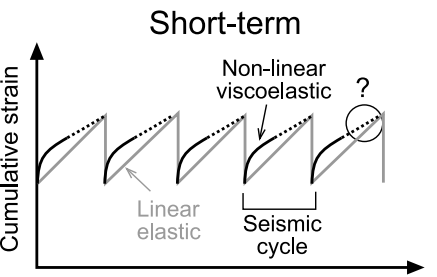

Seismic cycle time scale
(short-term < 10^2 years)

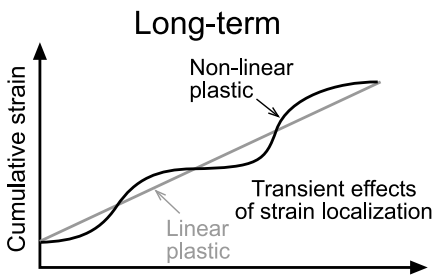

Tectonic time scale
(long-term > 10^5 years)

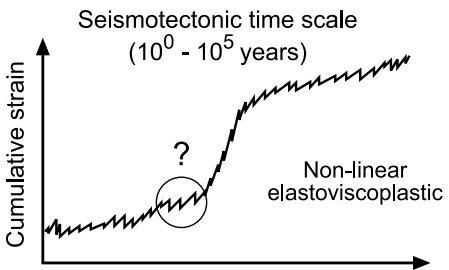

Dynamic experiment

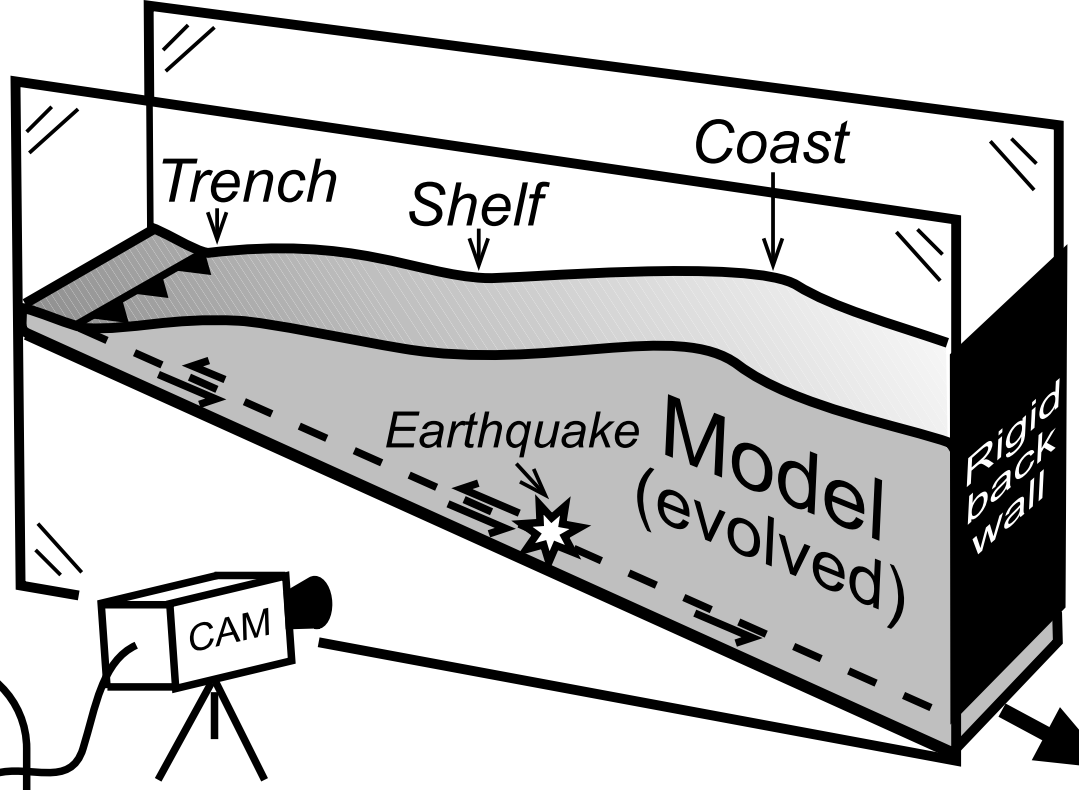

PIV
Strain analysis

motor-driven
conveyer plate

Output

Analog
earthquake
slip distribution

Input

EDM
Elastic dislocation
model

Output

Output

Elastoplastic
deformation pattern

Elastic
deformation pattern

Subtract

Plastic
deformation pattern
Residual

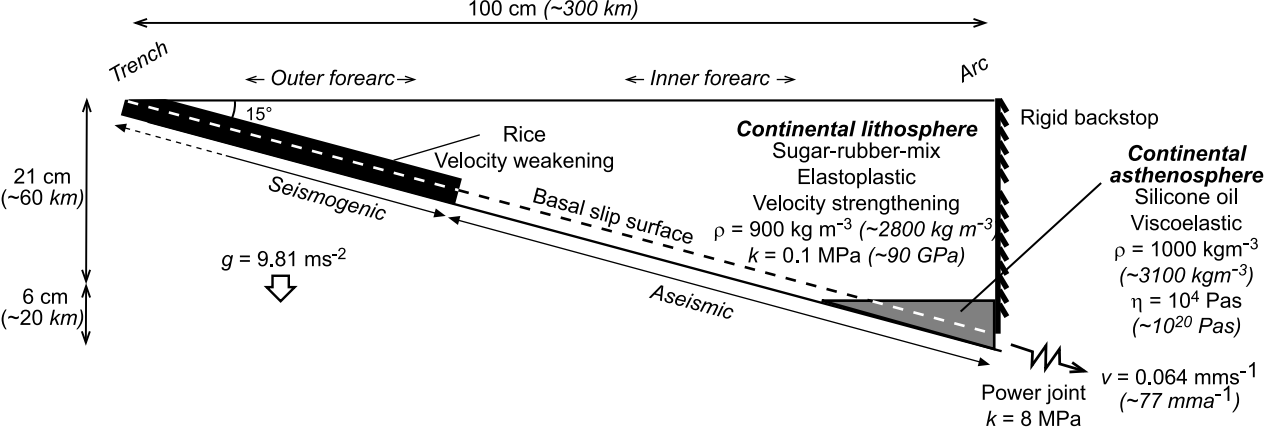
100 cm (~300 km)
Trench
← Outer forearc →
← Inner forearc →
Arc
15°
Rice
Velocity weakening
Seismogenic
Basal slip surface
Aseismic
Continental lithosphere
Sugar-rubber-mix
Elastoplastic
Velocity strengthening
ρ = 900 kg m-3 (~2800 kg m-3)
k = 0.1 MPa (~90 GPa)
Rigid backstop
Continental asthenosphere
Silicone oil
Viscoelastic
ρ = 1000 kgm-3
(~3100 kgm-3)
η = 10^4 Pas
(~10^20 Pas)
21 cm
(~60 km)
6 cm
(~20 km)
g = 9.81 ms-2
v = 0.064 mms-1
(~77 mma-1)
Power joint
k = 8 MPa

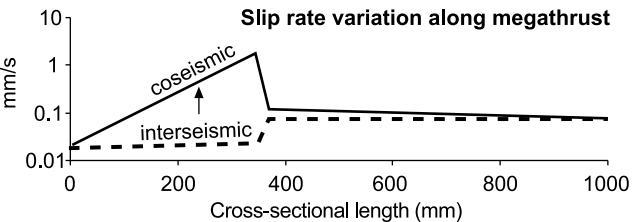
Slip rate variation along megathrust
mm/s
10
1
0.1
0.01
coseismic
interseismic
0
200
400
600
800
1000
Cross-sectional length (mm)

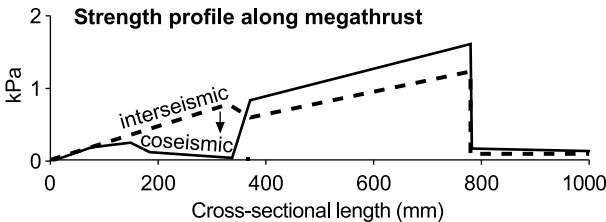
Strength profile along megathrust
kPa
2
1
0
interseismic
coseismic
0
200
400
600
800
1000
Cross-sectional length (mm)

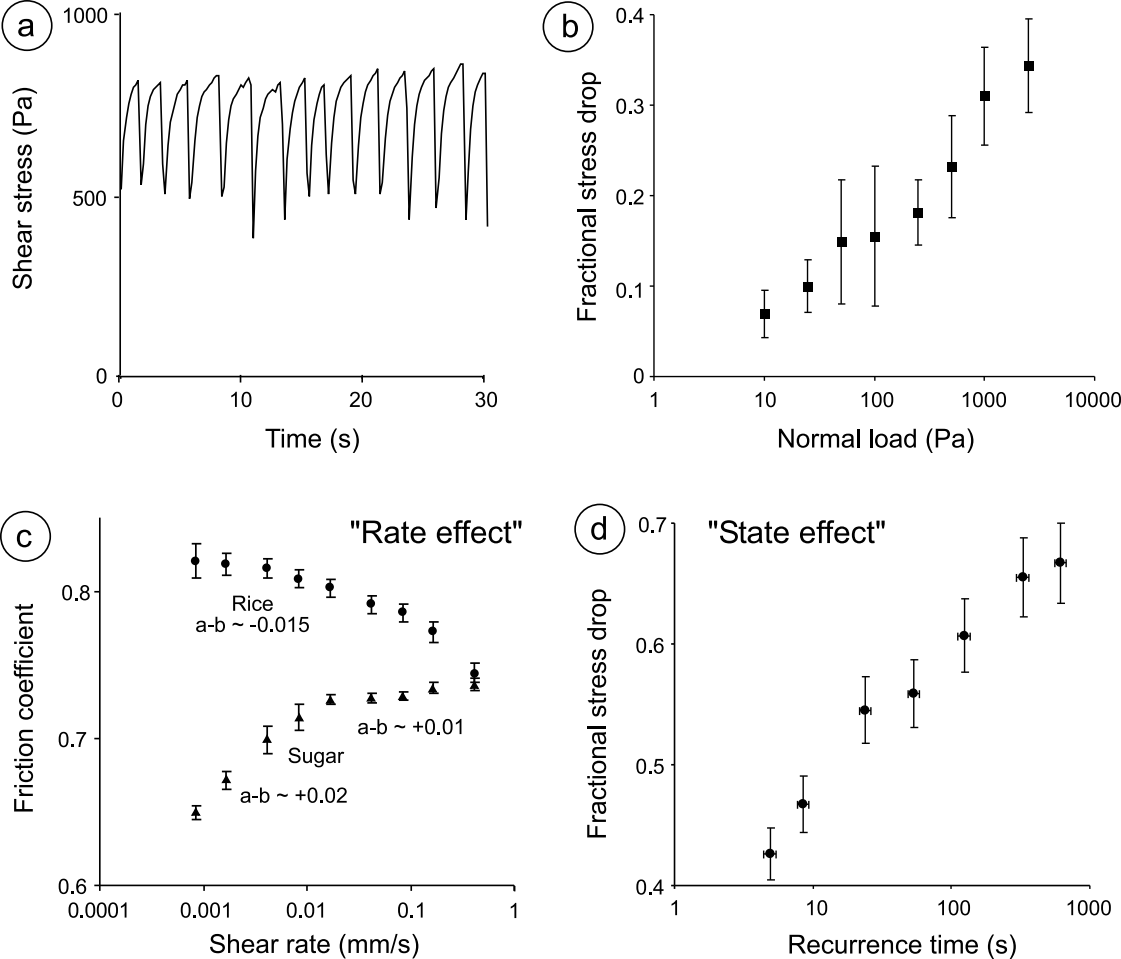
a
Shear stress (Pa)
1000
500
0
0
10
20
30
Time (s)
b
Fractional stress drop
0.4
0.3
0.2
0.1
0
1
10
100
1000
10000
Normal load (Pa)
c
"Rate effect"
Friction coefficient
0.8
0.7
0.6
Rice
a-b ~ -0.015
Sugar
a-b ~ +0.01
a-b ~ +0.02
0.0001
0.001
0.01
0.1
1
Shear rate (mm/s)
d
"State effect"
Fractional stress drop
0.7
0.6
0.5
0.4
1
10
100
1000
Recurrence time (s)

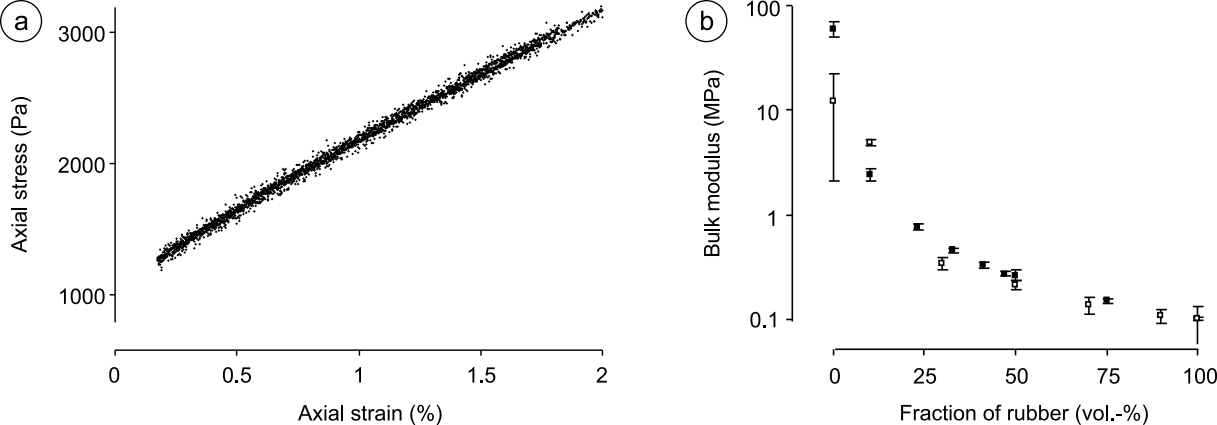
a
Axial stress (Pa)
3000
2000
1000
0
0.5
1
1.5
2
Axial strain (%)
b
Bulk modulus (MPa)
100
10
1
0.1
0
25
50
75
100
Fraction of rubber (vol.-%)

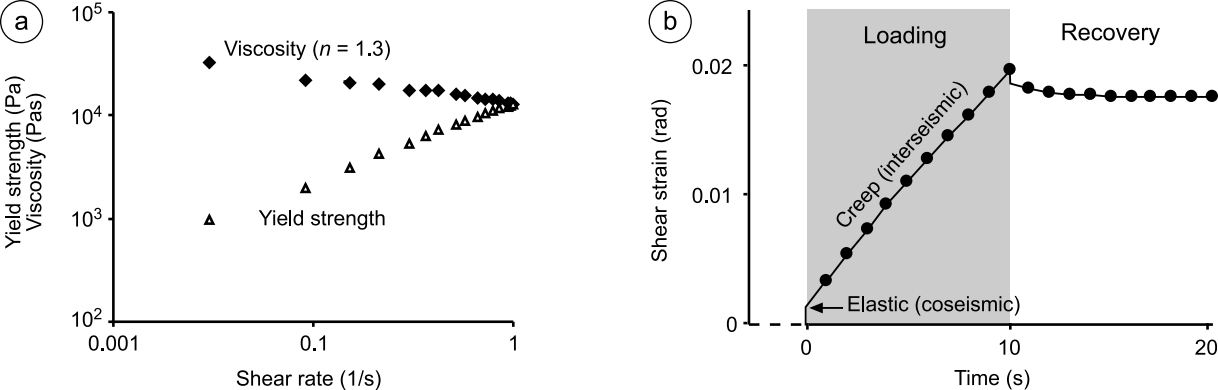
a
Viscosity (n = 1.3)
Yield strength
Yield strength (Pa)
Viscosity (Pas)
10^5
10^4
10^3
10^2
0.001
0.1
1
Shear rate (1/s)
b
Loading
Recovery
Creep (interseismic)
Elastic (coseismic)
Shear strain (rad)
0.02
0.01
0
0
10
20
Time (s)

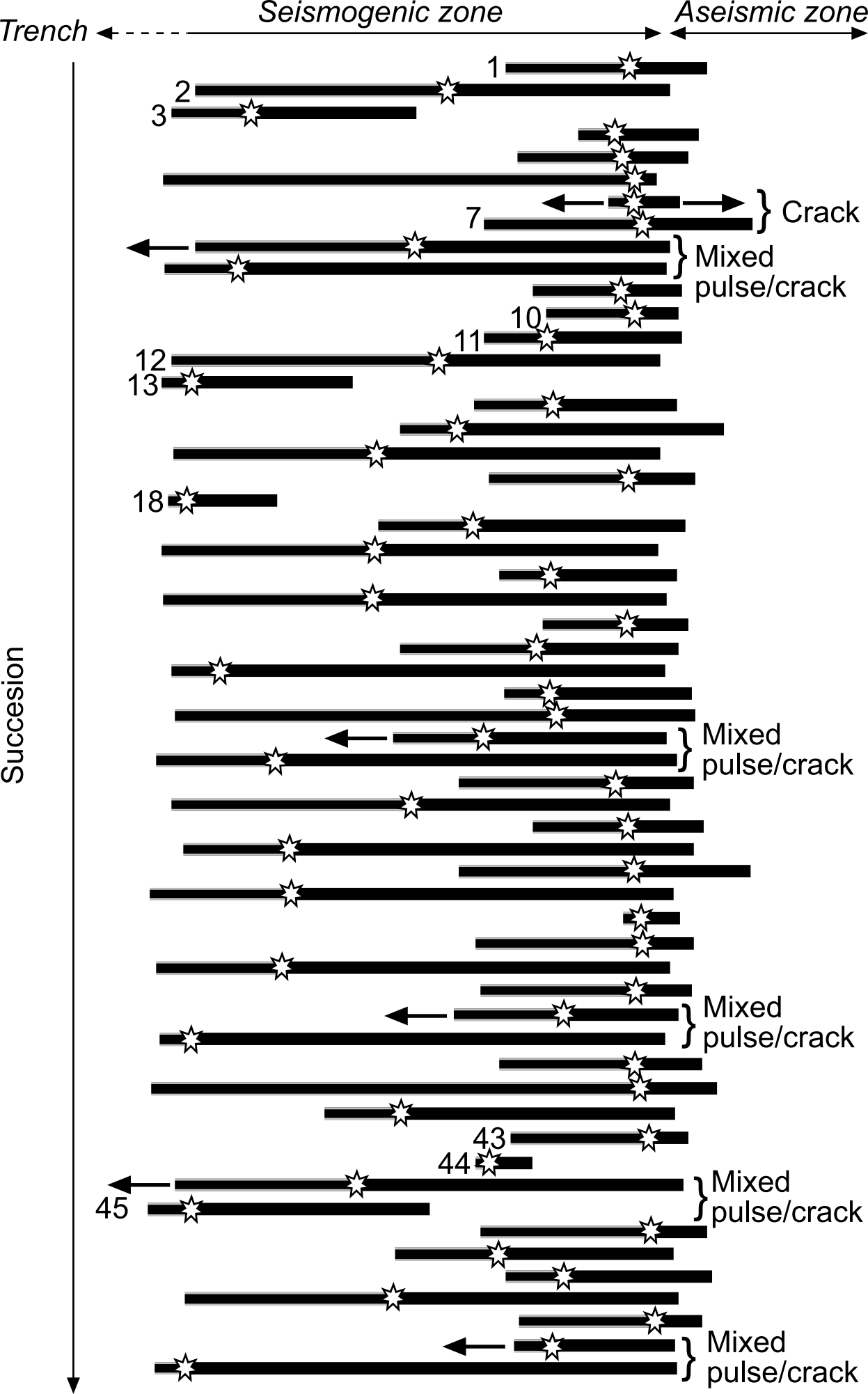
Trench
Seismogenic zone
Aseismic zone
Succesion
1
2
3
7
Crack
Mixed pulse/crack
10
11
12
13
18
Mixed pulse/crack
Mixed pulse/crack
43
44
45
Mixed pulse/crack
Mixed pulse/crack

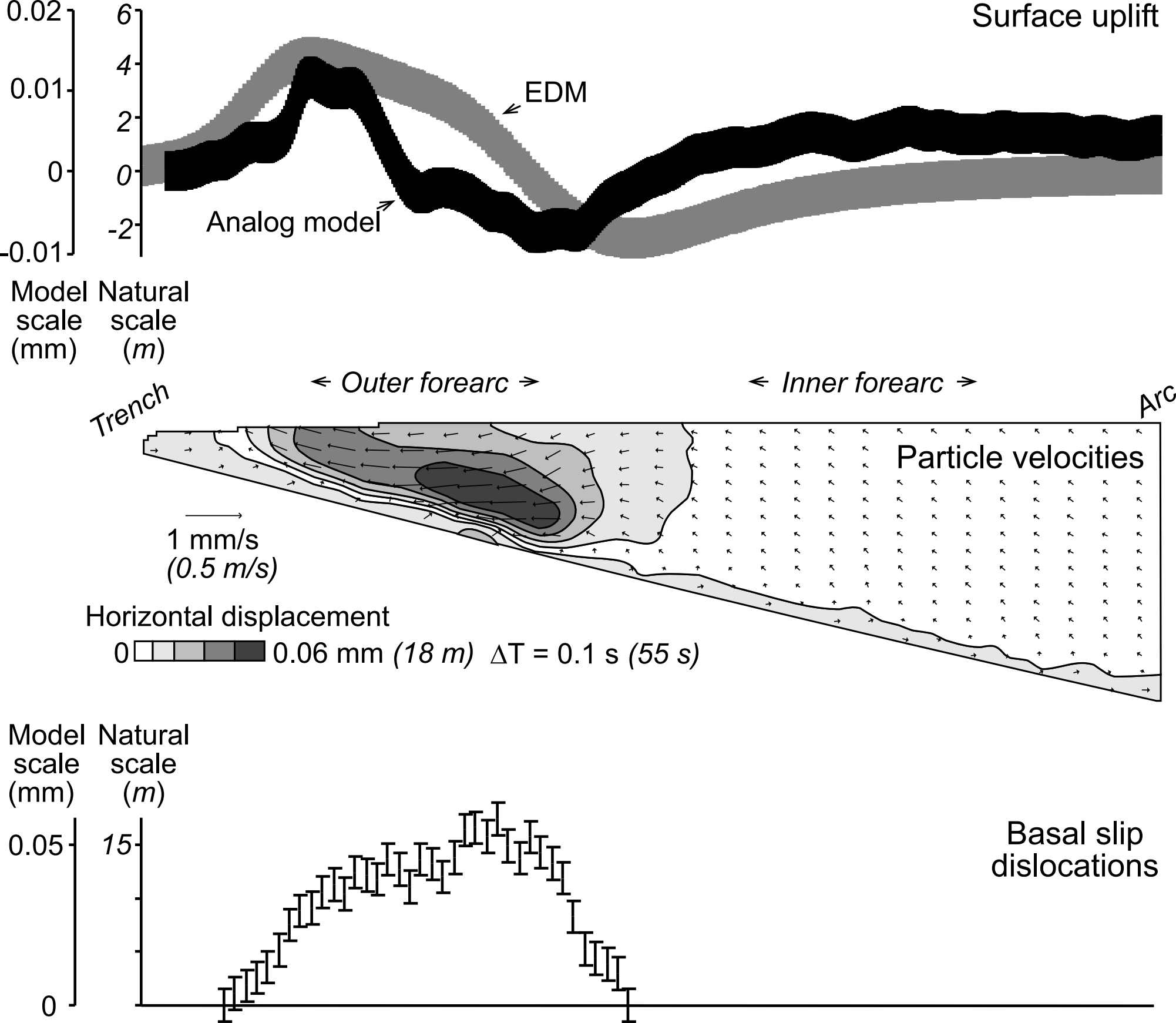
Surface uplift
0.02
0.01
0
-0.01
6
4
2
0
-2
EDM
Analog model
Model scale (mm)
Natural scale (m)
Trench
Outer forearc
Inner forearc
Arc
Particle velocities
1 mm/s
(0.5 m/s)
Horizontal displacement
0
0.06 mm (18 m) ΔT = 0.1 s (55 s)
Model scale (mm)
Natural scale (m)
0.05
0
15
Basal slip dislocations

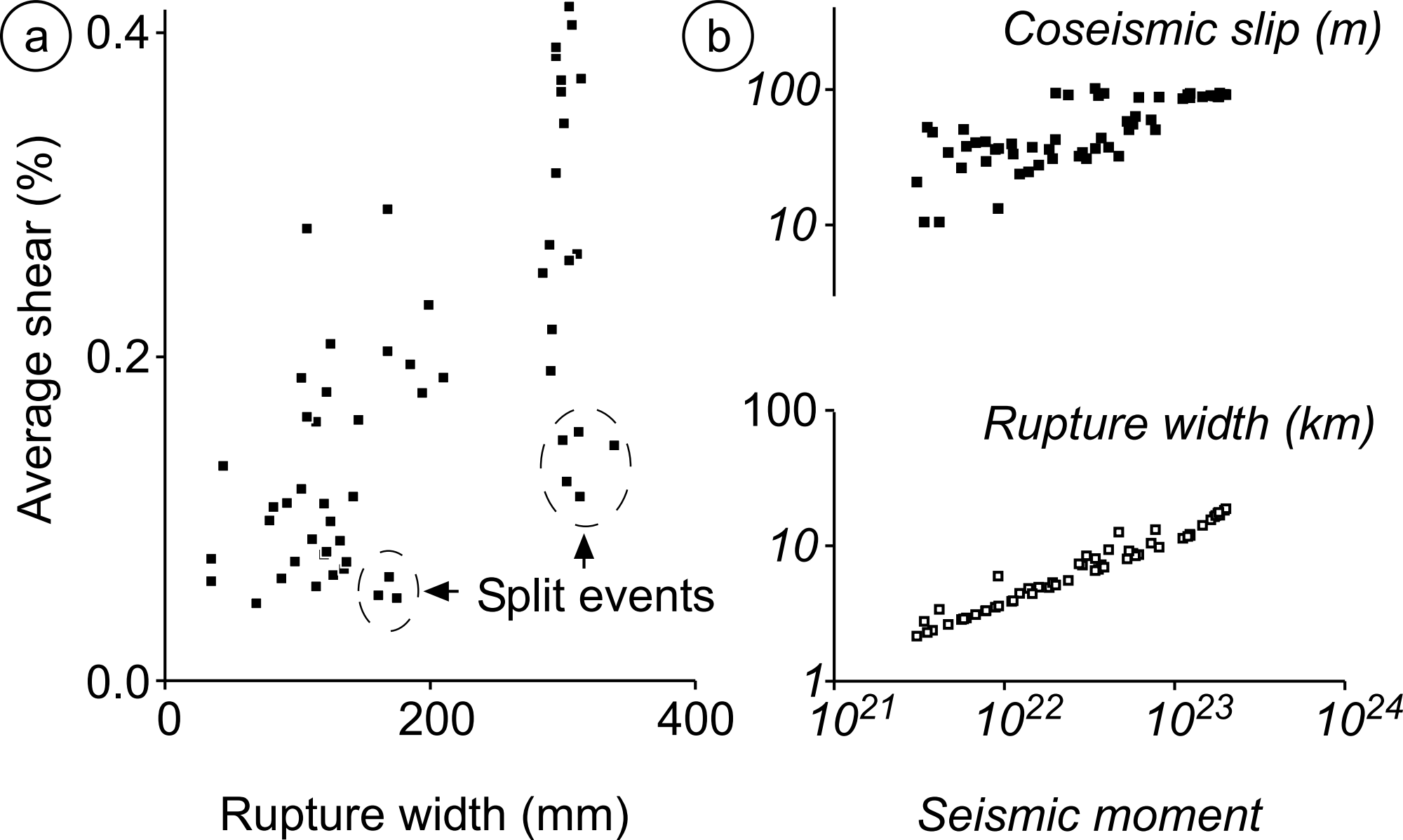
a
b
Average shear (%)
0.4
0.2
0.0
0
200
400
Split events
Rupture width (mm)
Coseismic slip (m)
100
10
100
10
1
Rupture width (km)
10^{21}
10^{22}
10^{23}
10^{24}
Seismic moment

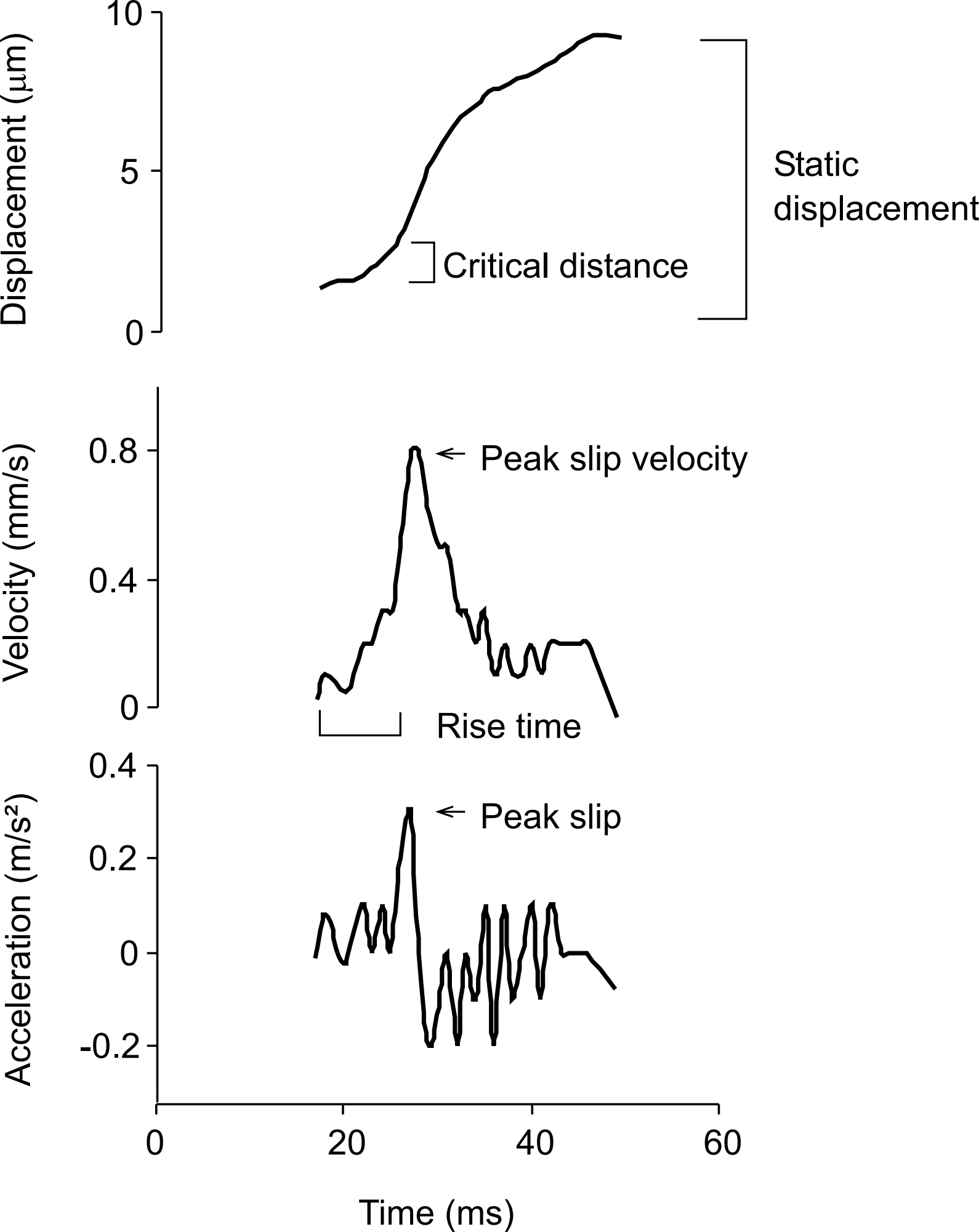
Displacement (μm)
10
5
0
Critical distance
Static
displacement
Velocity (mm/s)
0.8
0.4
0
Peak slip velocity
Rise time
Acceleration (m/s²)
0.4
0.2
0
-0.2
Peak slip
0
20
40
60
Time (ms)

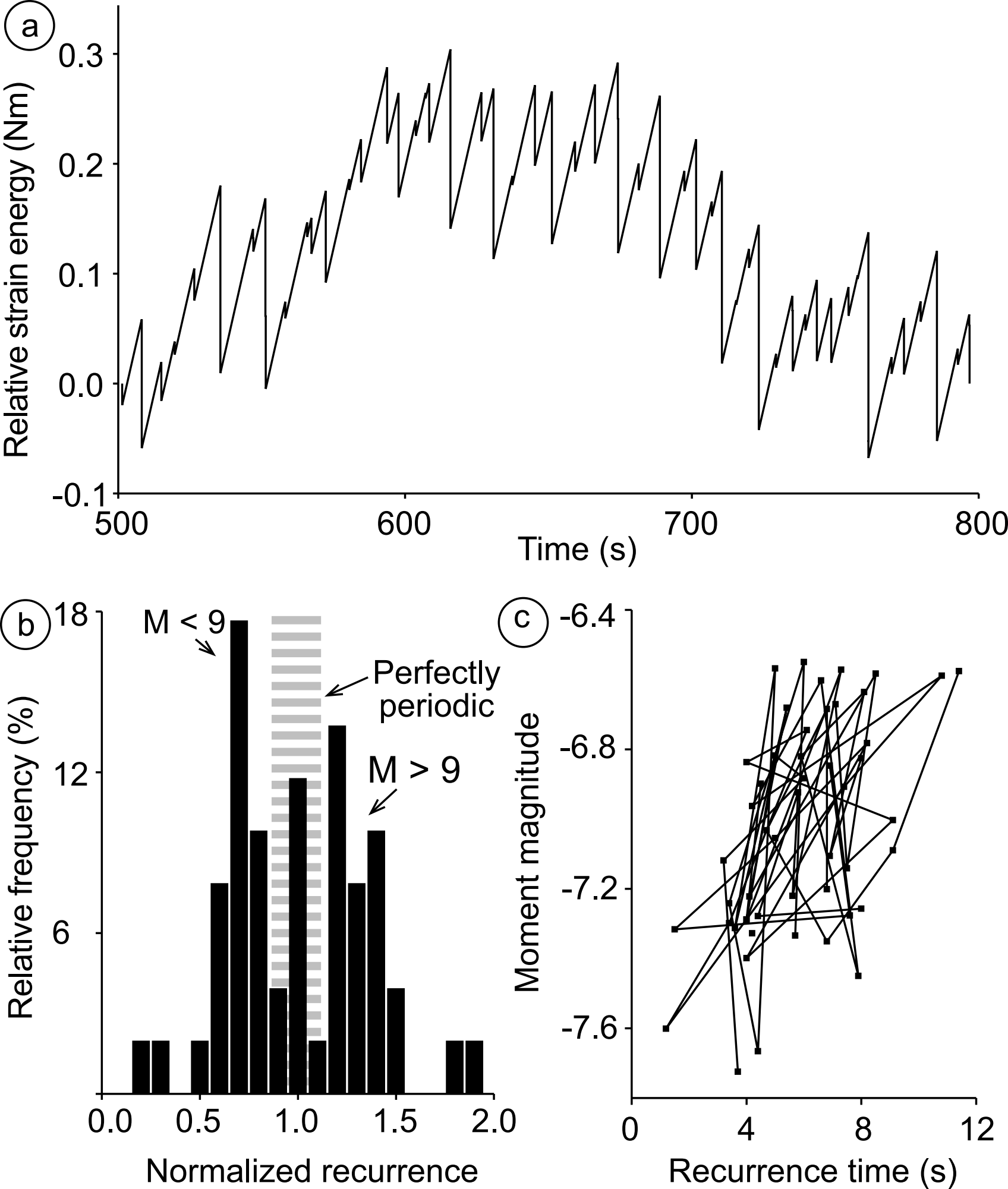
a
Relative strain energy (Nm)
0.3
0.2
0.1
0.0
-0.1
500
600
700
800
Time (s)
b
Relative frequency (%)
18
12
6
M < 9
Perfectly periodic
M > 9
0.0
0.5
1.0
1.5
2.0
Normalized recurrence
c
Moment magnitude
-6.4
-6.8
-7.2
-7.6
0
4
8
12
Recurrence time (s)

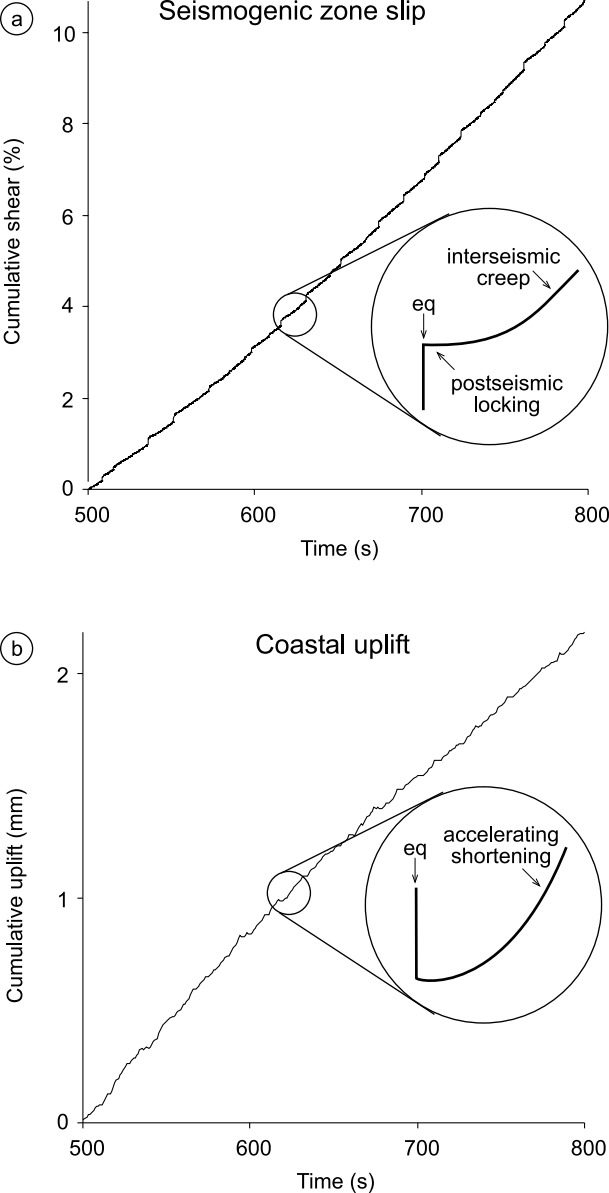
a
Seismogenic zone slip
Cumulative shear (%)
0
2
4
6
8
10
500
600
700
800
Time (s)
interseismic
creep
eq
postseismic
locking
b
Coastal uplift
Cumulative uplift (mm)
0
1
2
500
600
700
800
Time (s)
eq
accelerating
shortening

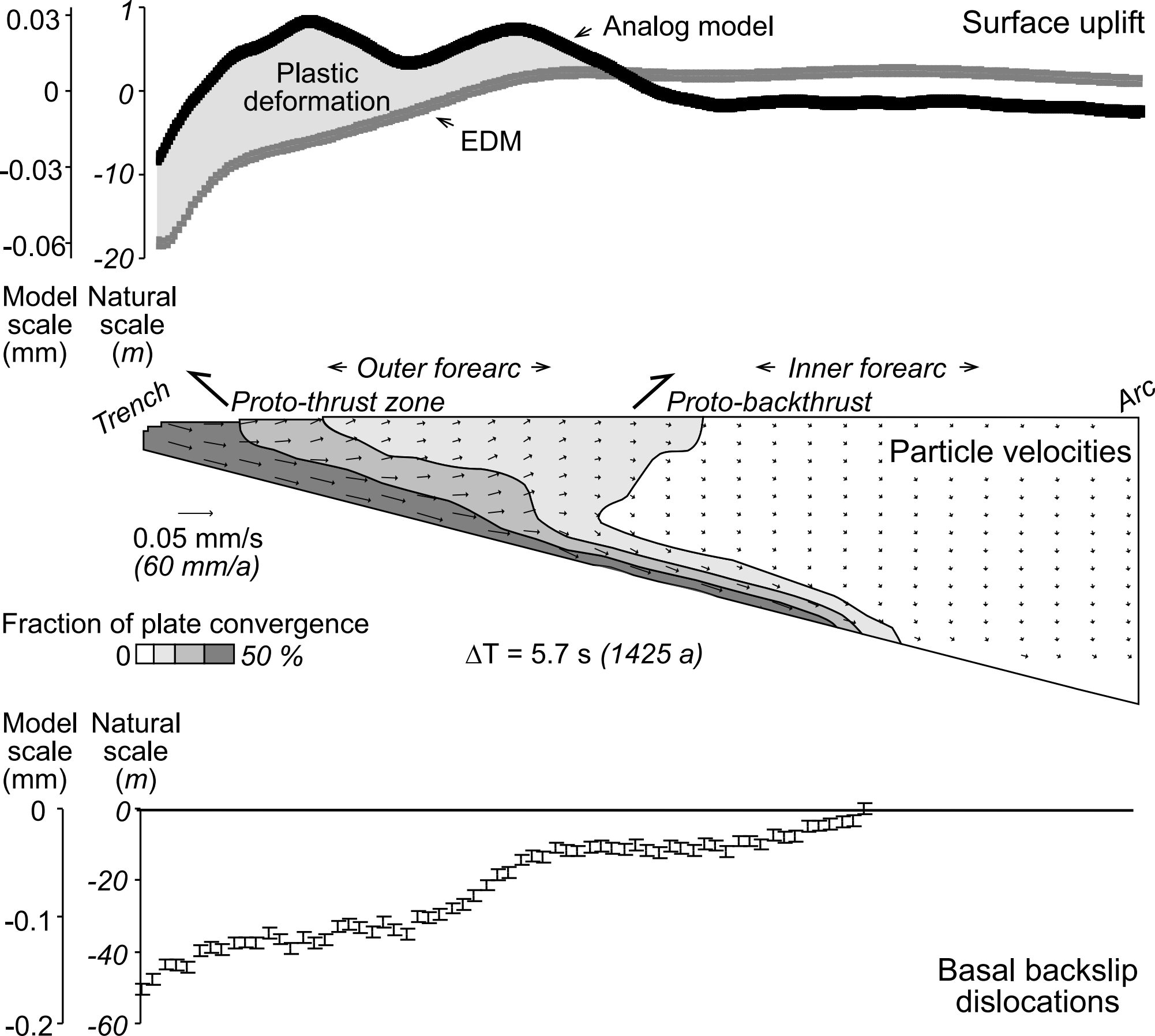
0.03
0
-0.03
-0.06
1
0
-10
-20
Plastic deformation
Analog model
EDM
Surface uplift
Model scale (mm)
Natural scale (m)
Outer forearc
Inner forearc
Trench
Proto-thrust zone
Proto-backthrust
Arc
Particle velocities
0.05 mm/s
(60 mm/a)
Fraction of plate convergence
0
50 %
ΔT = 5.7 s (1425 a)
Model scale (mm)
Natural scale (m)
0
-0.1
-0.2
0
-20
-40
-60
Basal backslip dislocations

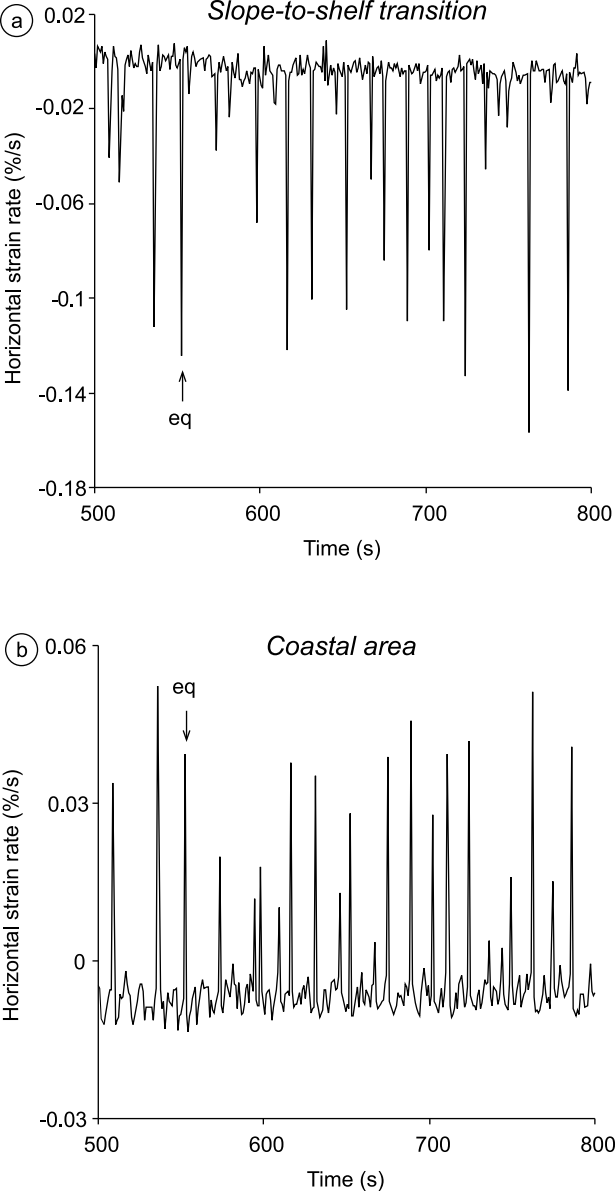
a
Slope-to-shelf transition
0.02
-0.02
-0.06
-0.1
-0.14
-0.18
Horizontal strain rate (%/s)
eq
500
600
700
800
Time (s)
b
Coastal area
0.06
0.03
0
-0.03
Horizontal strain rate (%/s)
eq
500
600
700
800
Time (s)

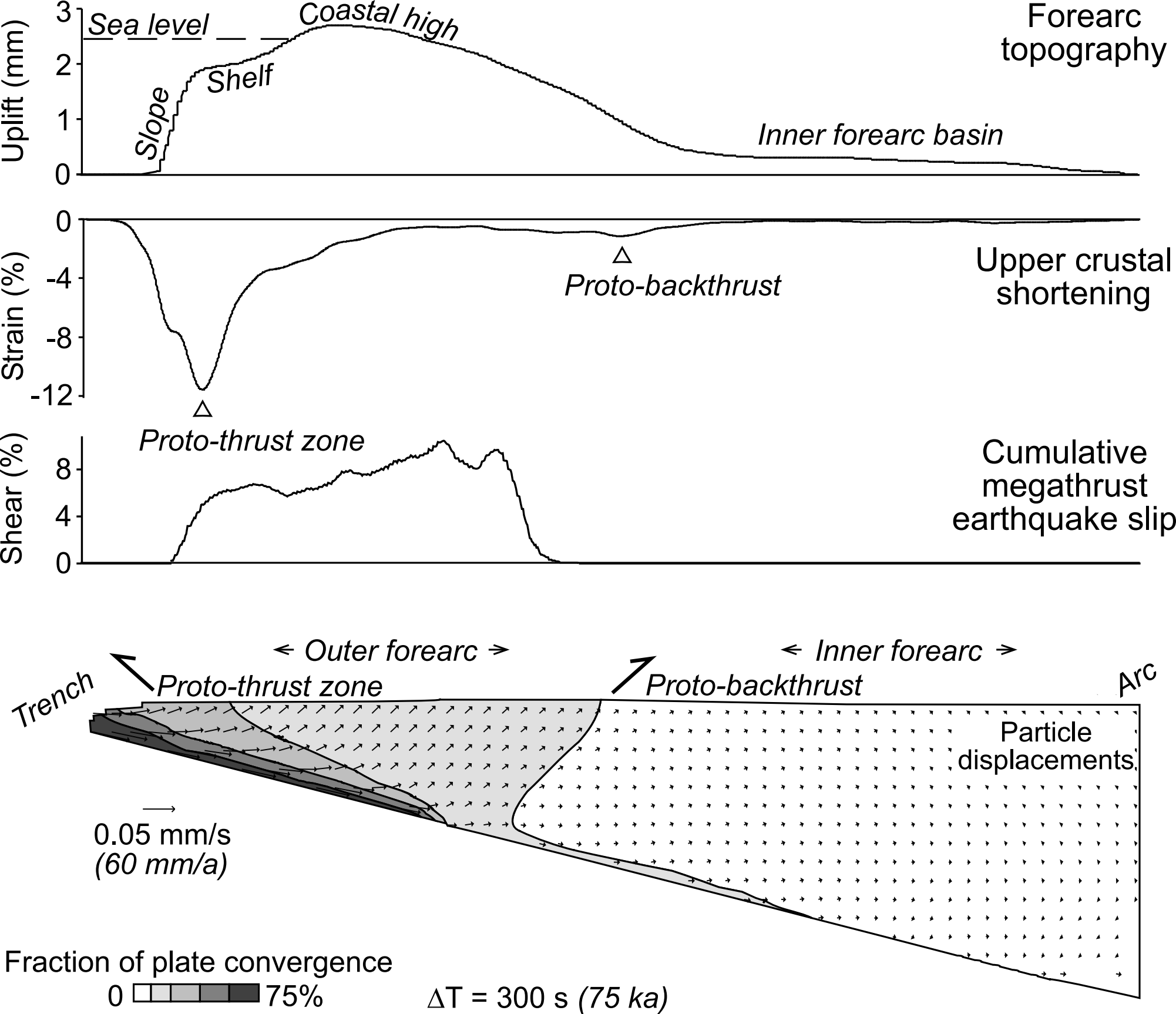
Uplift (mm)
3
2
1
0
Sea level
Coastal high
Shelf
Slope
Inner forearc basin
Forearc topography
Strain (%)
0
-4
-8
-12
Proto-backthrust
Upper crustal shortening
Proto-thrust zone
Shear (%)
8
4
0
Cumulative megathrust earthquake slip
Outer forearc
Inner forearc
Trench
Proto-thrust zone
Proto-backthrust
Arc
Particle displacements
0.05 mm/s
(60 mm/a)
Fraction of plate convergence
0
75%
ΔT = 300 s (75 ka)

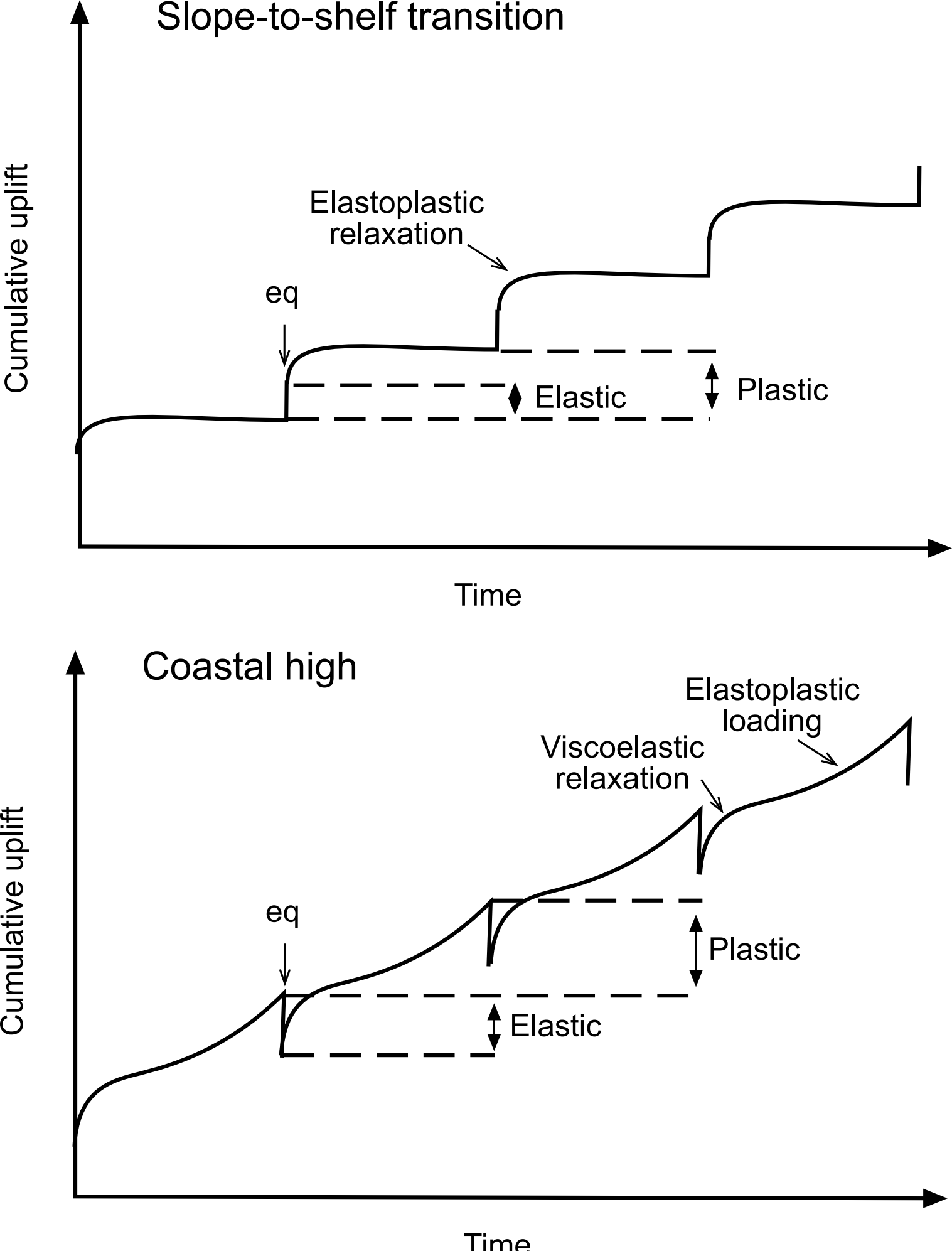
Slope-to-shelf transition
Cumulative uplift
Elastoplastic
relaxation
eq
Elastic
Plastic
Time
Coastal high
Cumulative uplift
Elastoplastic
loading
Viscoelastic
relaxation
eq
Plastic
Elastic
Time

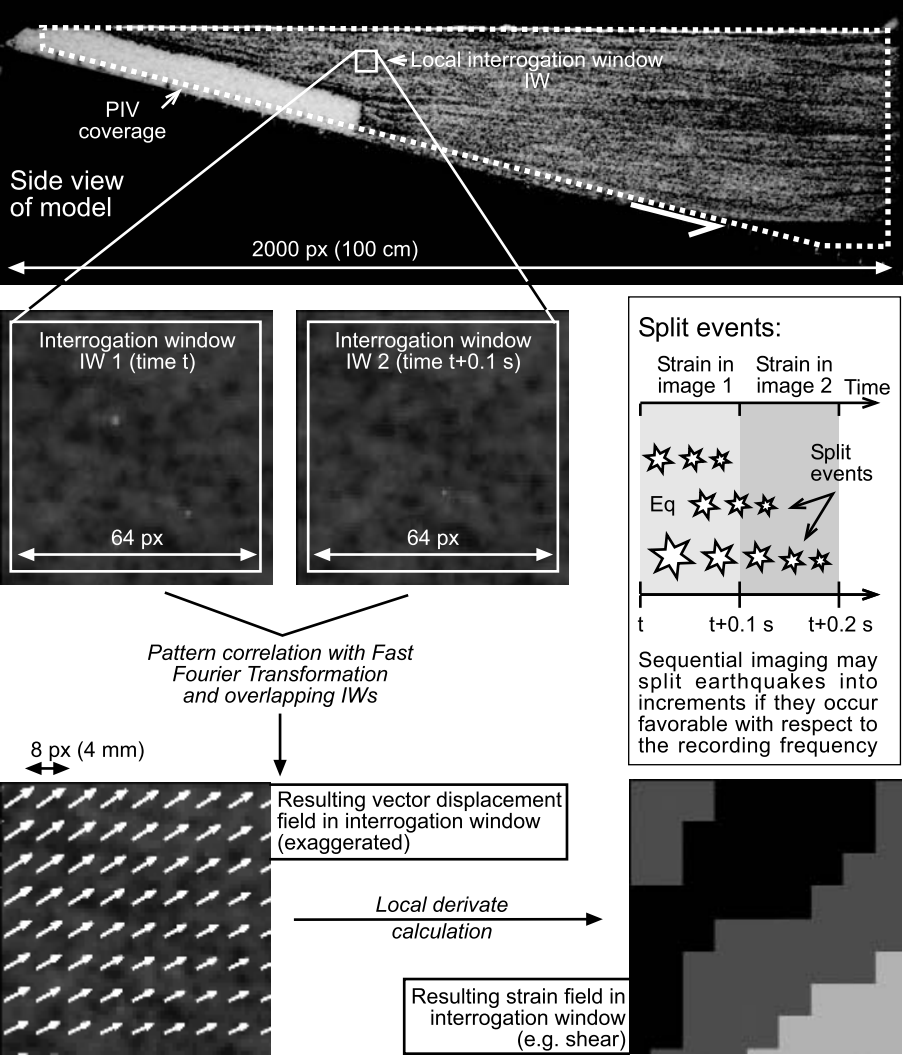
Local interrogation window
IW
PIV
coverage
Side view
of model
2000 px (100 cm)
Interrogation window
IW 1 (time t)
64 px
Interrogation window
IW 2 (time t+0.1 s)
64 px
Split events:
Strain in
image 1
Strain in
image 2
Time
Split
events
Eq
t
t+0.1 s
t+0.2 s
Sequential imaging may split earthquakes into increments if they occur favorable with respect to the recording frequency
Pattern correlation with Fast Fourier Transformation and overlapping IWs
8 px (4 mm)
Resulting vector displacement field in interrogation window (exaggerated)
Local derivate calculation
Resulting strain field in interrogation window (e.g. shear)